Title: Spatial periodicity of hippocampal place cells in navigation

Bo Zhang[1,2], and Jia Liu[2*]

[1] Beijing Academy of Artificial Intelligence, Beijing, 100084, China

[2] Tsinghua Laboratory of Brain and Intelligence & Department of Psychology, Tsinghua University, Beijing, 100084, China

*Correspondence shall be addressed to: JL, liujiathu@tsinghua.edu.cn

Abstract

To achieve the computational goal of navigating both natural and mental spaces, the brain employs a cognitive map, which is actualized by hippocampal place cells to encode locations of the map within a hexagonal coordinate system supplied by entorhinal grid cells. However, how this map is leveraged for navigational tasks remains unclear. Here, we designed an object-matching task where participants unknowingly manipulated object variants spatially arranged in a ring-like structure around a prototype. Functional neuroimaging revealed a spatial 3-fold periodicity in hippocampal activity during navigation, replicated across different groups. Importantly, this hippocampal periodicity was phase-locked with the well-documented 6-fold periodicity of entorhinal cortex, suggesting a holistic functional coupling between these regions. In light of this empirical evidence, we developed the E-H PhaseSync Model, which incorporates an algorithm formalizing the interplay of place cells' forward replay and grid cells' spatial axes, thereby generating a 3-fold periodic hippocampal vector field serving as a navigational guide. The implementation of the model not only reproduced participants' navigational behavior but also surprisingly predicted a 3-fold periodicity embedded in the behavior, which was substantiated by participants' behavioral data. Taken together, this study suggests that spatial periodicity originating from entorhinal grid cells serves as a bond to consolidate the hippocampal-entorhinal network, where the periodic hippocampal vector field emerges as the neural basis for utilizing the cognitive map in navigation.

Introduction

Cognitive map, proposed by Tolman (1948), denotes the mental space of conceptual knowledges coded by hippocampal place cells (O'Keefe & Dostrovsky, 1971; Epstein et al., 2017; Behrens et al., 2018; Park et al., 2020). Nevertheless, the mechanism by which the brain utilizes the cognitive map to execute path integration, a process metaphorically akin to knowledge retrieval and decision making, remains unclear. In a computational perspective, path integration relies on the winner-take-all dynamics (Bush et al., 2015; Bicanski and Burgess, 2019). Head direction cells might be the most well-known case, they preferentially fire in specific directions that dominate over all the others (Taube et al., 1990; Taube, 2007; Winter and Taube, 2014; Jeffery et al., 2016). Recently, Ormond and O'Keefe (2022) introduced the convergence sinks (ConSinks) of hippocampal place

cells, which are characterized by the vector fields that code allocentric directions and distances distributed throughout physical environment, and provide the maximal firing when animals are oriented towards the goal. The discovery of vector fields strongly corroborates the hypothesis of "Distance Cell" model (Bush et al., 2015), which assumes the "distance" cells akin to the ConSinks by calculating the vector from self- to goal-location and reaching the goal with increasing activity. In together, those empirical evidences suggested the capacity of place cells in vector-based representation using winner-take-all dynamics, which provides the navigational signal to achieve the goal. In this context, the functionality of hippocampal vector fields might be interpreted as being equivalent to those inherent in the cognitive map (Jeffery, 2007; Colgin et al., 2008).

How the vector fields, that represent the direction from self-body to goal, are formed? One of the possible origins would be the entorhinal grid cells (Hafting et al., 2005). Anatomically, the entorhinal cortex (ERC) provides major projections terminated in the subiculum, CA1, and CA3 fields of the downstream hippocampus (HPC), where place cells reside (Witter & Amaral, 1991; van Groen et al., 2003; Garcia and Buffalo, 2020). Functionally, place cells remap environment in concert with the spatial realignment of grid fields (Fyhn et al., 2007), while complete lesion to ERC results in a substantial disruption of place representation in precision and stability (Hales et al., 2014). Those discoveries suggested a major effect of ERC on hippocampal place codes. Particularly, the hexagonal metric of grid cells, identified in physical (Hafting et al., 2005), object (Constantinescu., 2016), visual (Nau et al., 2018), odor (Bao et al., 2019), reward (Sosa and Giocomo, 2021) and sequential space (McNamee et al., 2021), presumably serves as the foundation to construct the relation of spatial locations. Computationally, the formation of place field, hypothesized by the "grid cell to place cell" model, relies on the linear summation of two or more grid modules, and the representation of a place cell for a given location can be encoded by the phase vector of grid modules (Solstad et al., 2006; de Almeida et al., 2009; Bush et al., 2014; Bush et al., 2015; Bicanski and Burgess, 2019). Although the model well explained the presence of place codes with either single or multiple firing fields, it is clearly not capable with the interpretation of vector field formation in direction coding (Ormond and O'Keefe, 2022).

We hypothesized that ERC-HPC circuitry transmits the direction signals via periodic codes. In classic discovery of Hubel and Wiesel (Hubel and Wiesel, 1959; Hubel and Wiesel, 1962), the

ganglion cell activity in the striate cortex of rats is modulated by a moving light spot, suggesting the capacity of neurons in coding spatial information relative to the field of view independent to temporal domain (see also Bieri et al., 2014; Fiebelkorn et al., 2018). Similarly, grid cells exhibited spatial periodicity to tessellate spatial environment with orientation and spacing almost invariant at populational level (Hafting et al., 2005; Stensola et al., 2015; Krupic et al., 2015; Gardner et al., 2022). Beneficial with this property, the hexagonal signals of grid cell, characterized by the 6-fold periodic pattern modulated by conceptual directions (Doeller et al., 2010; Constantinescu et al., 2016; Bao et al., 2019), have been stably detected under fMRI (functional Magnetic Resonance Imaging) scanning, which measures metabolic changes across thousands of individual neurons at millimeter level, thus offering a broader scope of brain scanning relative to electrophysiology. In Ormond and O'Keefe (2022), a large proportion of hippocampal ConSink cells showed significant encoding of both spatial direction and distance. Inspired from those studies, we questioned that whether the neural activity of hippocampal place cells is predictable by periodic manner? If so, we expected to observe the neural periodicity in HPC, which should show significant modulation with spatial directions independent to temporal domain and phase-locked to the entorhinal grid cells.

To test the hypothesis, we developed an object matching task, which requires participants to morph the object variants by button press to match the target prototype they learned prior to the experiment (Fig.1). Unbeknownst to participants, they navigated in a 2-dimensional conceptual space, constituted by the length of two object components, namely "Vacso" and "Loogit". In each trial, participants started to "move" from the periphery of space (start locations, yellow dots) and stopped at the center where the prototype was situated (goal location, blue dot). All participants fully explored the space from all start locations, each location corresponded to a unique conceptual direction towards the goal. We found a robust 3-fold modulation in the CA1 of HPC, where the BOLD signals fluctuated as a function of directions, confirming the spatial periodicity of HPC. Moreover, the BOLD activity series in the HPC significantly phase-coupled with the 6-fold periodicity observed in the ERC, presumably reflecting the signal transmissions from grid to place cell ensembles. To confirm it, we built the "E-H PhaseSync" model to simulate path integration based on Entorhinal-Hippocampal phase synchrony. As the result, the vector field representations were self-emerged by hippocampal place cells, and exhibited 3-fold periodicity in travel directions. To ensure the robustness of HPC periodicity in direction coding, we identified significant 3-fold

modulation in task performance of human participants, which was predictable by the phase of hippocampal BOLD activity series. In together, those results provided evidences in explaining the formation of hippocampal vector fields from the hexagonal metric of grid cells.

Results

Construction of a conceptual object space

A novel 3D object, named greeble (Gauthier and Tarr, 1997; Fig.1a), was used to construct a conceptual object space. Within this space, a location in the space (Fig.1c) represents a unique greeble variant characterized by distinct length of its two components that form the two dimensions of the space, namely "Loogit" and "Vacso." The greeble in the center of the space was the prototype, serving as the target. In each trial, a greeble variant, randomly selected from the periphery of the space (Fig.1c, the red point within the ring-shaped orange area), was presented on screen. Participants were instructed to adjust the length of Loogit and Vasco independently via button press to match the prototype as accurately as possible (Fig.1b). This process generated a navigational trajectory constituted by a sequence of selected greeble variants (i.e., locations; Fig.1c). To ensure comprehensive exploration of the object space, greeble variants were evenly sampled such that participants experienced conceptual directions ranged from 0° to 360° relative to the goal location (see Methods for details). Note that no participant was aware of the existence of the object space or had a subjective feeling of navigating during the experiment. To mitigate the impact of learning effects on BOLD signals of MRI scanning, participants were trained one day prior to the MRI experiment (see Fig.S1 for details). As a result, all participants performed the task well, and the probability density map of the ending-locations across trials had a peak at the prototype (Fig. 1d).

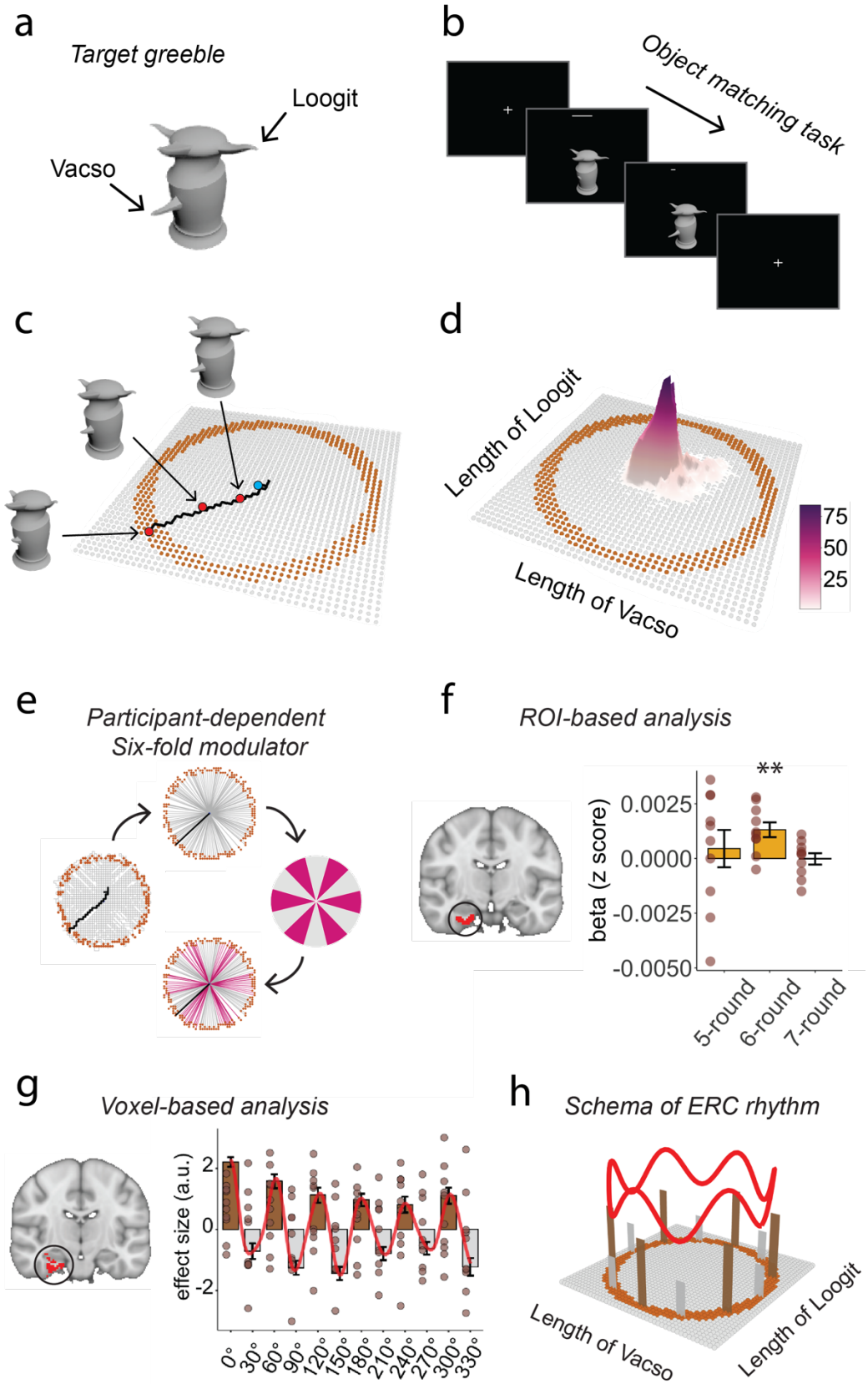
a
Target greeble
Loogit
Vacso
b
Object matching task
c
d
Length of Loogit
Length of Vacso
75
50
25
e
Participant-dependent
Six-fold modulator
f
ROI-based analysis
**
beta (z score)
0.0025
0.0000
-0.0025
-0.0050
5-round
6-round
7-round
g
Voxel-based analysis
effect size (a.u.)
2
0
-2
0°
30°
60°
90°
120°
150°
180°
210°
240°
270°
300°
330°
h
Schema of ERC rhythm
Length of Vacso
Length of Loogit

Figure 1. Experimental design and 6-fold modulation in the Entorhinal cortex. a) Depiction of the greeble prototype and its two defining components, namely "Loogit" and "Vacso." b) Within the MRI scanner, participants continuously adjusted the length of Loogit and Vacso to match the prototype by button press within a 10-s time limit. c) Conceptual object space. Each orange dot within the ring-shaped area represents a variant greeble, while the central blue dot indicates the prototype greeble (i.e., the goal location). Red dots denote intermediate locations along the navigational trajectory (i.e., the black line). d) Distribution of the ending-locations, aggregated across participants. e) Schematic detailing the six-fold modulator for localizing grid cell activity. Participants' trajectories were simplified to straight lines connecting the starting and the ending locations, which were further classified into either "aligned" or "misaligned" conditions. f) ROI-based analysis, with an anatomical mask manually delineated from the MNI template, replicated the 6-fold modulation of BOLD signals in comparison to both 5- and 7-fold modulations. g) Voxel-based sinusoid analysis revealed grid cell activity within the right ERC (peak MNI coordinate: 19, -15, -27; peak t = 4.58). h) Three-dimensional schema illustrating the relationship between the 6-fold modulation in the ERC and conceptual directions within the object space.

Six-fold modulation in the ERC and 3-fold modulation in the HPC

In the fMRI analysis, we first identified the entorhinal hexagonal activity when participants implicitly navigated in the object space. With the sinusoidal analysis (Fig.1e, see Methods for details), we revealed significant uniformity of grid orientations (Fig.S3, $p < 0.05$, Rayleigh test of uniformity, Bonferroni corrected), and identified a significant activity cluster in the right ERC (Fig.1g; $p < 0.01$, initial threshold; $p < 0.05$, small-volume cluster-corrected (SVC) for multiple comparisons; Cohen's $d = 0.7$), corresponding to the 6-fold modulation of the hexagonal pattern of grid cells, characterized by a 60° periodicity. In contrast, no significant clusters were detected corresponding to 5-fold (72° periodicity) or 7-fold (51.4° periodicity) modulations. An additional ROI analysis with an anatomical ERC mask corroborated the robustness of the 6-fold modulation (Fig.1f, $t(9) = 3.89$, $p = 0.003$; Cohen's $d = 1.2$), not the 5- or 7-fold modulations (Fig.1f, 5-round: $t(9) < 1$, 7-round: $t(9) < 1$). These results confirmed the involvement of entorhinal grid cells in the object-matching task, consistent with previous findings (e.g., Doeller et al., 2010).

Anatomically, the HPC receives afferent projections from the ERC (Witter & Amaral, 1991; van Groen et al., 2003; Garcia and Buffalo, 2020), suggesting the potential for observing periodical neural activity patterns in the HPC. To test this intuition, our experimental design mandated that participants explored a full range of conceptual directions, ranged from 0° to 360° in increments of 1°, allowing the examination of hippocampal spatial periodicities of neural activities in addition to the established 60° periodicity. Specifically, we employed spectral analysis (see Methods for detail), which obviates the need for the prior hypothesis on periodicity or phase-offset calibrations as necessitated by sinusoid analysis (Doeller et al., 2010; Constantinescu et al., 2016), to explore periodicity spectrum within the medial temporal lobe (MTL). In this analysis, conceptual directions were down-sampled into 15° bins, generating a vector of resampled directions (e.g., 0°, 15°, and 30°), thereby enabling the detection of frequencies up to 11 Hz. A Fast Discrete Fourier Transform (FFT) was performed on the direction-dependent activity series, as estimated by GLM and sorted in ascending order (Fig.2a). Spectral power was then extracted for each voxel, ranging from 0 Hz to 11 Hz. As a result, we observed a significant cluster with an FFT magnitude centered at 3 Hz within the anterior portion of the right HPC (Fig.2b; $p < 0.05$, initial threshold; $p < 0.05$, SVC for multiple comparisons; Cohen's $d = 0.9$). Visual inspection further indicated that this peak magnitude at 3 Hz was presented in the CA1 region of the HPC (Iglesias et al., 2015). Additionally, the direction-dependent activity series, extracted via an anatomical mask of the anterior HPC,

showed a discernible 3-fold periodic pattern that fluctuates as a function of conceptual directions (Fig.2c & d). Taken together, our spectral analysis successfully identified a robust 3-fold periodicity located in the CA1 region of the HPC.

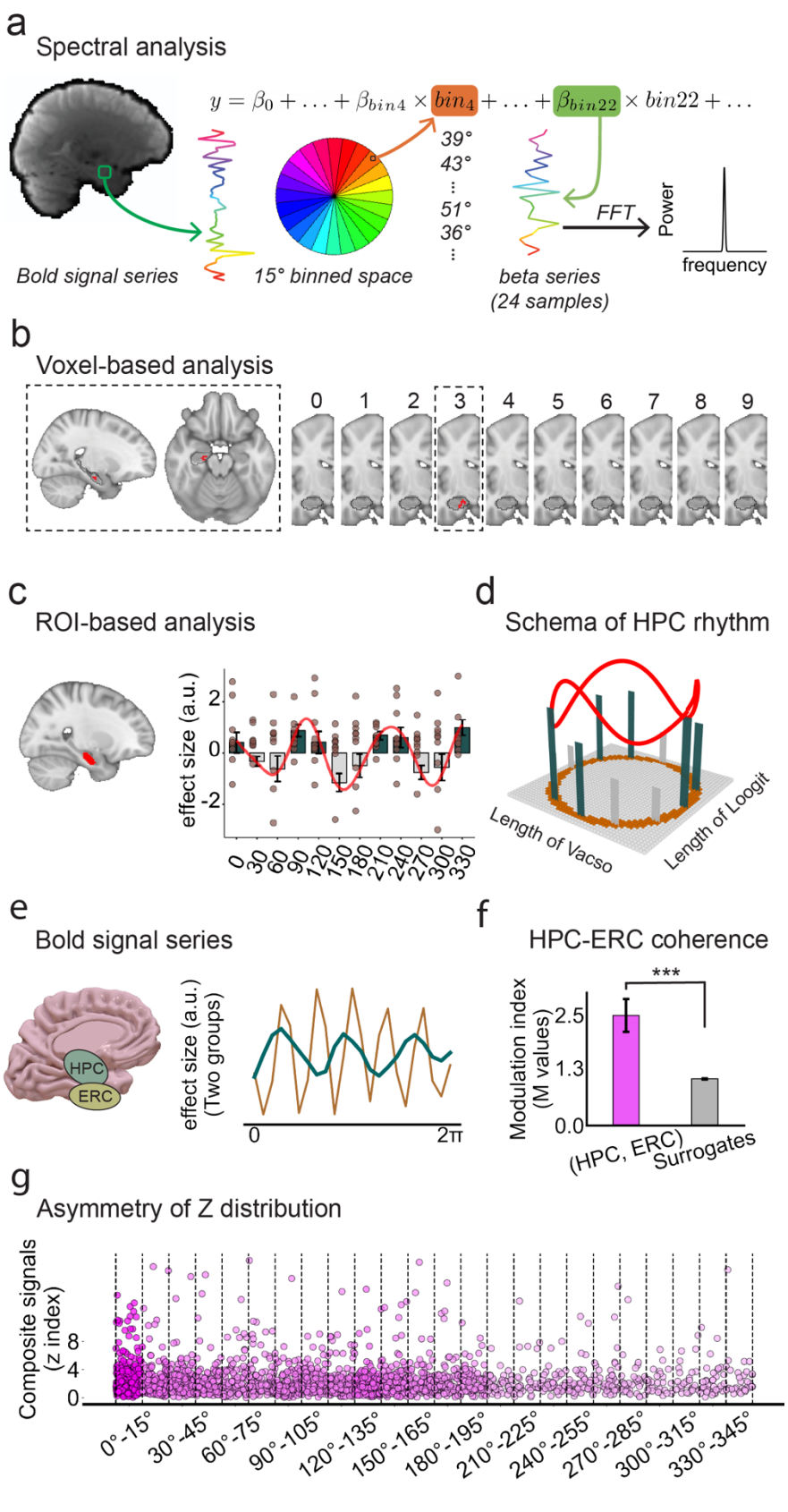
a
Spectral analysis
$y = \beta_0 + \ldots + \beta_{bin4} \times bin_4 + \ldots + \beta_{bin22} \times bin22 + \ldots$
39°
43°
51°
36°
FFT
Power
frequency
Bold signal series
15° binned space
beta series
(24 samples)
b
Voxel-based analysis
0 1 2 3 4 5 6 7 8 9
c
ROI-based analysis
effect size (a.u.)
2
0
-2
0 30 60 90 120 150 180 210 240 270 300 330
d
Schema of HPC rhythm
Length of Vacso
Length of Loogit
e
Bold signal series
HPC
ERC
effect size (a.u.)
(Two groups)
0
2π
f
HPC-ERC coherence
***
Modulation index
(M values)
2.5
1.3
0.0
(HPC, ERC)
Surrogates
g
Asymmetry of Z distribution
Composite signals
(z index)
8
4
0
0°-15°
30°-45°
60°-75°
90°-105°
120°-135°
150°-165°
180°-195°
210°-225°
240°-255°
270°-285°
300°-315°
330°-345°

Figure 2. Three-fold modulation in the HPC and its synchronization with 6-fold modulation in the ERC. a) Schema illustrating the procedure of spectral analysis to identify neural periodicities within the MTL. b) Voxel-based spectral analysis revealed a significant 3-fold modulation in the right HPC (Peak MNI coordinate: 20, -14, -18). c) The 3-fold modulation of the HPC based on the anatomical mask of bilateral HPC. **: $p < 0.01$. d) Three-dimensional schema illustrating the relationship between the 3-fold modulation in the HPC and conceptual directions within the object space. e) Visual inspection on the averaged time series of bold activity, extracted from anatomical masks of the HPC (depicted in green) and the ERC (yellow), showed a phase-locked pattern. f-g) Amplitude-phase coupling analysis on the ERC and HPC activity series corroborated the significant coherence of HPC and ERC activity series, suggested by f) the significantly higher modulation index M as compared to that of surrogates ($t(19)=3.77$, $p<0.001$) and g) the asymmetric distribution of composite z values as a function of the spatial directions. Note that the probability density (denoted by color scale) showed the strongest density (darker purple) at the 0°-15° bin, consistent with the observation of the phase shift. Error bars indicate SEM.

The hippocampal 3-fold modulation has not been previously reported in the spatial domain either by neurophysiological or fMRI studies. To validate the reliability of this finding, we therefore recruited a completely new group of participants (i.e., the replication group) and conducted the experiment at a different imaging center. The experimental design, data preprocessing and analyses remained identical with the original experimental group. In short, we replicated all major findings reported earlier (Fig.S4). That is, we found the involvement of grid cells in the right ERC (Fig.S4a, $p < 0.01$, initial threshold; $p < 0.05$, SVC for multiple comparison; Cohen's $d = 0.7$), and also identified the 3-fold modulation in the CA1 region of the right HPC (Fig.S4b, $p < 0.05$, initial threshold; $p < 0.05$, SVC for multiple comparison; Cohen's $d = 3.3$). The results in the replication study substantiate the reliability of the 3-fold modulation observed in the HPC.

To further examine our intuition that the observed periodic neural activity in the HPC may originate from the periodic activity of grid cells in the ERC, we investigated whether the phases of these two periodic activities were synchronized. To do this, we extracted the BOLD series from each participant and from each of the ERC and HPC, using data derived from sinusoid and spectral analyses, respectively. Visual inspection shows that 80% of the participants exhibited discernible

phase-locked patterns (Fig.S6), characterized by the overlapping peaks of 3-fold and 6-fold periodicities (Fig.2e). To corroborate the observation, an amplitude-phase modulation analysis was employed to quantify the extent of cross-frequency coherence between the ERC and HPC. Specifically, the amplitude envelope from high-frequency activity series in the ERC and the phase of low-frequency activity series in the HPC were extracted. The composite signal z was constructed at each sample point through $z = A_{ERC}e^{i\phi_{HPC}}$ (Canolty et al., 2006). The modulation index M was derived by computing the mean of vector Z for the composite signal series and permutated surrogates of each participant. This analysis revealed a significantly higher modulation strength relative to surrogate controls (Fig. 2f; $t(19)=3.77$, $p<0.001$), suggesting a coherence between the ERC and HPC. Moreover, the radial asymmetry observed in the probability density function of Z indices signifies the presence of shared mutual information encoded in specific phases (i.e., spatial directions) between the ERC and HPC (Fig.2g). Notably, the highest density of Z indices was found within the 0°-15° bin ($p < 0.05$, corrected for multiple comparisons), fitting nicely with the observed phase shift shown in Fig. 2e. Taken together, both visual inspection and statistical analysis indicated that peaks in the ERC activity series selectively aligned with those in the HPC activity. Note that this result differs from prior work in the temporal domain, where neural activity coherence is typically characterized by the modulation of low-frequency bands on high-frequency signals (e.g., Kahana et al., 2001; Uhlhaas and Singer, 2002). Rather, our results may reflect a causal link between the formation of 3-fold periodicity of place cells and the 6-fold periodicity of grid cells, despite the variability in the phase of activity series across participants (Fig.S6).

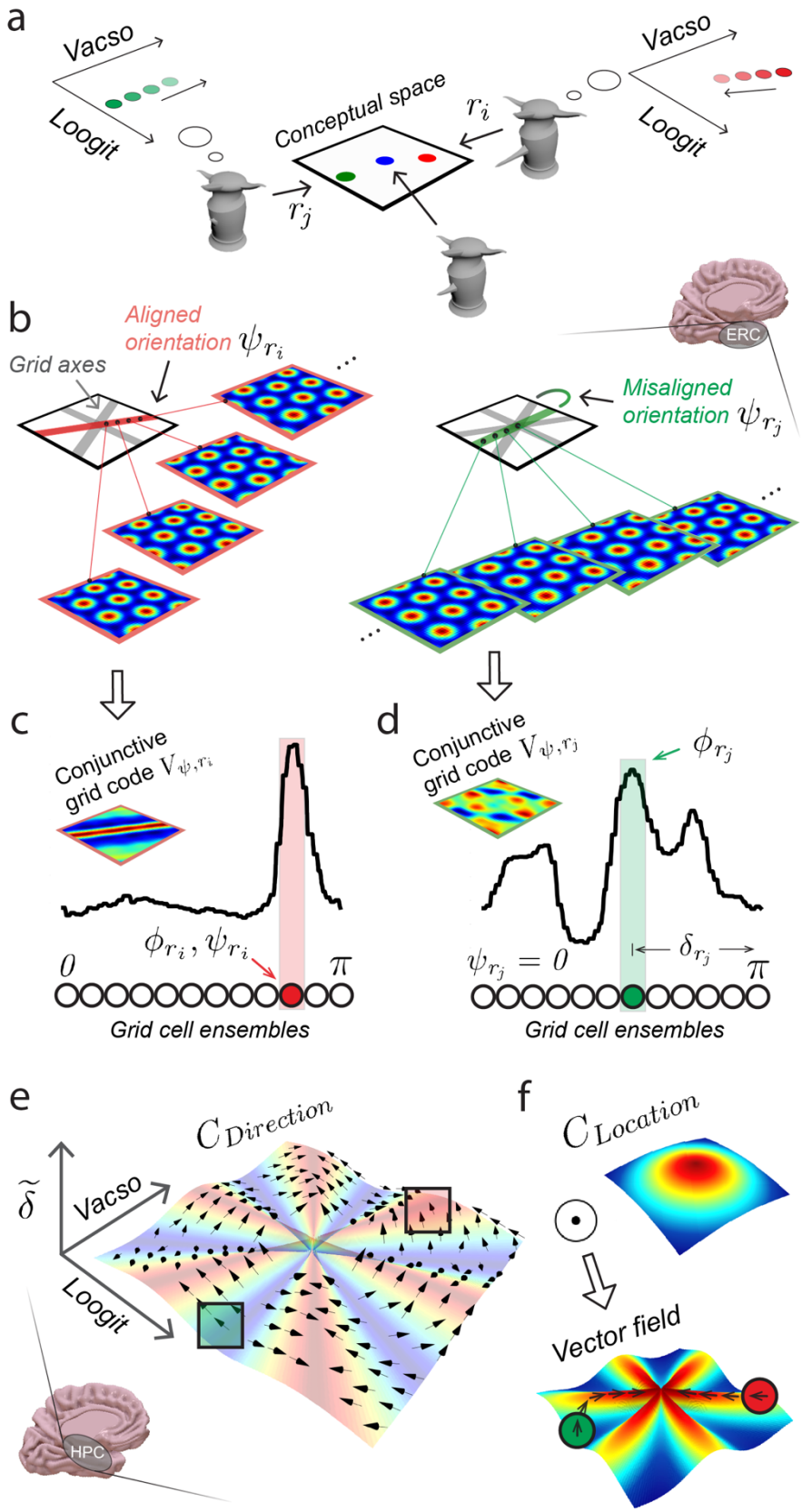
a
Vacso
Loogit
Conceptual space
r_i
r_j
Vacso
Loogit
b
Aligned orientation ψ_{r_i}
Grid axes
ERC
Misaligned orientation ψ_{r_j}
c
Conjunctive grid code V_{ψ,r_i}
ϕ_{r_i}, ψ_{r_i}
0
π
Grid cell ensembles
d
Conjunctive grid code V_{ψ,r_j}
ϕ_{r_j}
$\psi_{r_j} = 0$
δ_{r_j}
π
Grid cell ensembles
e
$C_{Direction}$
$\tilde{\delta}$
Vacso
Loogit
HPC
f
$C_{Location}$
Vector field

Figure 3. Computational Model for the Formation of Hippocampal Vector Field. a) Path planning for two greeble variants is shown, originating from respective self-location r_i (red dot) and r_j (green dot) toward the goal (blue dot) in the object space. b) Global directions ψ_{r_i} (red line) and ψ_{r_j} (green line), derived from the path planning for the greebles at locations r_i and r_j, respectively, activate different sets of grid cell ensembles along their respective paths. Note that global direction ψ_{r_i} (red line) is assumed to align with one of the primary axes of the grid cell ensemble, whereas ψ_{r_j} (green line) does not. c) Head direction ϕ_{r_i} is derived from the conjunctive grid code V_{ψ,r_i} formulated by the grid cell ensemble along the global direction ψ_{r_i}. Head direction ϕ_{r_i} is ascertained by the direction with maximum activity among reconstructed directions ranging from 0 to π. In this example, since global direction ψ_{r_i} aligns with one of the primary axes of the grid cell ensemble, the head direction ϕ_{r_i} is equivalent to the global direction ψ_{r_i}. d) Conversely, global direction ψ_{r_j} does not align with any primary axis of the grid cell ensemble; therefore, the head direction ϕ_{r_j} (green filled rectangle) no longer equals to the global direction ψ_{r_j}. e) Construction of hippocampal direction map $C_{Direction}$. For each self-location r within the space, its head direction ϕ_r is compared to its global direction ψ_r, resulting in a difference δ_r (i.e., $\phi_r - \psi_r$) with smaller values of δ_r correspond to higher levels of activity in $C_{Direction_r}$. In this example, self-location r_i (red filled rectangle) and r_j (green filled rectangle) correspond to a large and smalle δ, respectively. Note that hippocampal direction map $C_{Direction}$ shows a 3-fold periodicity. $\tilde{\delta}$ denotes the normalized δ. f) Formation of vector field map C is achieved by integrating $C_{Direction}$ with $C_{Location}$ that proximity to the target corresponds to elevated activity levels. Accordingly, a greeble variant moves from its self-location to the goal by recursively navigating toward the location with maximal surrounding activity.

The "E-H PhaseSync" Model

To elucidate the mechanism by which the hexagonal firing pattern of grid cells in the ERC projects onto place cells in the HPC to give rise to the observed 3-fold periodicity in the HPC, we developed a computational model, termed the "E-H PhaseSync" model. This model is predicated on an intuition that the 3-fold modulation observed in the HPC may be intrinsically linked to the three primary axes of the hexagonal firing pattern of grid cells through a process of phase-locking (Buzsaki, 2006; Guanella et al., 2007; Gardner et al., 2022). This intuition is supported by previous studies that underscores the invariance of grid orientation and spacing at the population level in the biological brain (Hafting et al., 2005; Stensola et al., 2015; Krupic et al., 2015; Gardner et al., 2022).

The "E-H PhaseSync" model first simulates path planning from a starting location r within the conceptual 2D space (Fig.3a) by employing spatial imagining (Buckner, 2010; Mullally and Maguire, 2014). The spatial imagining, known as "forward replay", reflects the capacity of an individual place cell to activate a sequence of spatially adjacent place cells (Diba and Buzsáki, 2007; Dragoi and Tonegawa, 2011; Pfeiffer, 2020). The sequence of locations, indicated by the activated place cells, forms a global direction ψ_r that extends from the starting location r to the goal within the space (Diba and Buzsáki, 2007; Dragoi and Tonegawa, 2011; Pfeiffer, 2020). Accordingly, grid cells along this global direction ψ_r are activated (Fig. 3b), an ensemble of hexagonal firing patterns. By linearly combining the grid code ensemble, conjunctive representation $V_{\psi,r}$ of the location sequence is constructed by $\exp\left(\sum_i G_{r_{i,\psi}}\right)$, where $G_{r,\psi}$ represents the grid code of location r and ψ denotes the global direction (Fig. 3c & d). Note that when the global direction aligns with one of primary axes of grid cells, the conjunctive representation V_ψ exhibits characteristics similar to plane waves (Fig.3c), which have been previously identified in the medial ERC of freely moving rats (Welday et al., 2011, Krupic et al., 2012). In contrast, when the head direction does not align with the grid axes, irregular multi-peak patterns emerge, leading to suboptimal directional choices in relation to the goal (Fig.3d).

With the conjunctive representation $V_{\psi,r}$, the head direction ϕ_r at location r is extracted. Specifically, an activity vector $f(\psi)$ is introduced to represent the distribution of direction preferences around the location r (Equation 1), where each direction preference is determined by

summing the activities of $V_{\psi,r}$ across the j locations along the global direction ψ (Johnson et al., 2005; see Methods for details). Note that ψ is ranged from 0 to π due to the symmetry of the space.

$$f(\psi) = \mathcal{Z}[\{\sum_{j} V_{\psi,r_j}\}_{\psi=0}^{\pi}] \quad (1)$$

Head direction ϕ_r is identified by locating the maxima of $f(\psi)$ (Fig.3c & 3d). When the global direction ψ_r aligns with one of the primary axes of the grid cell ensemble, the head direction ϕ_r coincides with the global direction, yielding an angular difference δ_r of 0 (Fig. 3c). Conversely, when ψ_r does not align with any primary axis of the grid cell ensemble, ϕ_r diverges from ψ_r, resulting in a δ_r greater than 0 (Fig.3d). Therefore, a smaller value of δ_r, signifying greater similarity between the head direction and the global direction, elicits a stronger activity $C_{Direction_r}$ from the place cell at the location r. For example, the activity of the place cell at r_i is higher than that at r_j (Fig.3c & 3d).

By aggregating $C_{Direction_r}$ across locations in the space, a hippocampal direction map $C_{Direction}$ is formulated, which is based on place cells' neural activity. Given that the activity of an individual place cell is modulated by the grid cell ensemble, the resultant activities of place cells vary as a function of global directions, which establishes three vector-based attractors at the population level (Fig.3e). That is, the 3-fold spatial periodicity observed in the fMRI study is likely an emergent property that arises when the hexagonal periodicity of grid cells is inherited by hippocampal place cells. Finally, by additionally incorporating the distance map $C_{Location}$, where closer proximity to the target correlates with higher activity of the corresponding place cell (Bush et al., 2015; Ormond and O'Keefe, 2022), the hippocampal vector field C is generated (Fig.3f; Equation 2).

$$C_r = C_{Location_r} \odot C_{Direction_r} \quad (2)$$

Utilizing the above-mentioned computational model, C at location r provides a navigation vector relative to the agent's current location. That is, the agent at a given location is poised to transition to the adjacent location exhibiting the highest activity of C_r.

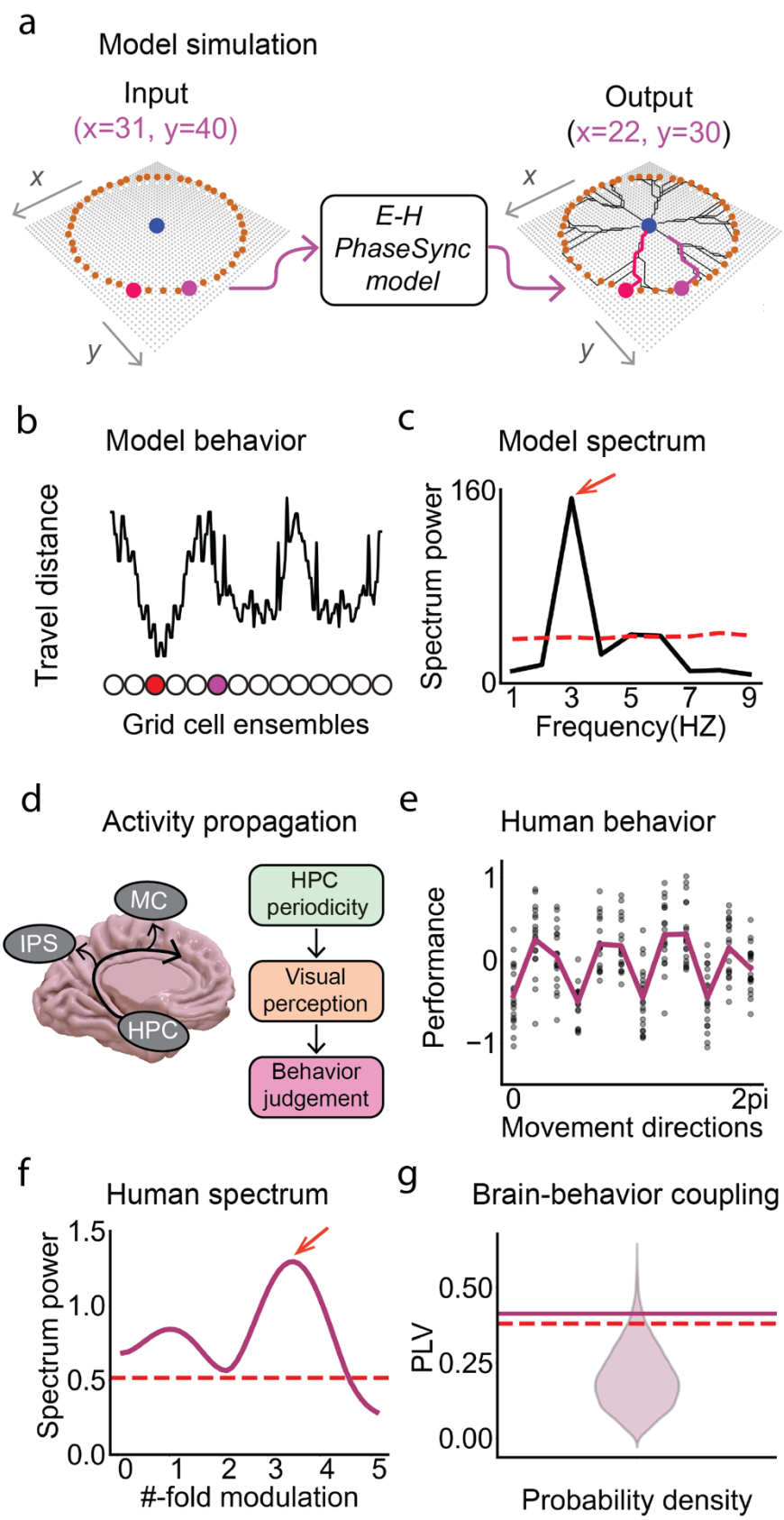
a
Model simulation
Input
(x=31, y=40)
Output
(x=22, y=30)
x
y
E-H
PhaseSync
model
b
Model behavior
Travel distance
Grid cell ensembles
c
Model spectrum
Spectrum power
160
0
1
3
5
7
9
Frequency(HZ)
d
Activity propagation
MC
IPS
HPC
HPC
periodicity
Visual
perception
Behavior
judgement
e
Human behavior
Performance
1
0
−1
0
2pi
Movement directions
f
Human spectrum
Spectrum power
1.5
1.0
0.5
0.0
0
1
2
3
4
5
#-fold modulation
g
Brain-behavior coupling
PLV
0.50
0.25
0.00
Probability density

Figure 4. Periodic performance characteristics of the ERC-to-HPC model and human participants. a) Implementation of the E-H PhaseSync model, which receives the self-location on the object space as input and outputs the next location towards the goal. Forty-five starting-locations, that form a ring-shaped pattern, outcome 45 trajectories for illustration purpose. The red and purple exemplar trajectories denote the paths with global directions either aligning or misaligning with the primary grid axis, respectively. b) Model performance, measured by the travel length in each trial as a function of global directions. Note that when the head direction, as provided by the grid cell ensemble, aligned with the global direction, the resultant travel length was shorter (red) compared to instances of misalignment (purple), thereby manifesting as periodic fluctuations in the performance of path integration. c) Three-fold modulation of the model's behavioral performance as revealed by spectral analysis. The red line indicates the baseline derived from a permutation analysis for each frequency, while the red arrow highlights the peak of the behavioral spectrum. d) Schema of the hypothesis that the task performance of human, govern by the visual-motor system of brain, is associated with the 3-fold modulation of HPC. e) Human performance, measured by a composite index of the path length and the discrepancy between the intended goal location and the achieved endpoint, at each movement direction. Note that participants' performance fluctuated periodically as a function of movement directions. f) Three-fold modulation of human performance with a significant spectral power at a frequency of 3.36 Hz. The red line indicates the power baseline derived from the permutation analysis across frequencies. g) Phase-phase coherence between participants' behavioral performance and HPC activity time series. The Phase-Lock Value (PLV, purple line) between the performance and HPC activity exceeded the 95th percentile of the PLV distribution obtained from randomly shuffled surrogates (red dashed line).

3-fold modulation in model and human behavior

In consideration of the periodic structure of the vector field C in the model, it becomes inevitable that the anisotropic pattern in directional preferences will substantially impact the model's performance in path integration. That is, contrary to the commonly held assumption of an isotropic directional pattern in hippocampal place cells, the travel length from the starting location to the goal is shorter when the global location aligns with the primary grid axes, as compared to instances of misalignment. To test this prediction, we implemented the E-H PhaseSync" Model, wherein an agent performed the object matching task as human participants did. In each path of the simulation, agent's self-location was initialized from one of the starting-location set (Fig.4a; orange dots). The model receives the coordinate of self-location as input, and outputs the next location to update the original self-location until the goal is reached. As expected, the anisotropic pattern of the agent's trajectories emerged across the conceptual space, a result attributable to the directional anisotropy in the vector field C (Fig.4a; "output" panel). Indeed, the travel length originated from each starting location fluctuated periodically as a function of global directions, each of which was uniquely encoded by a specific ensemble of grid cells during path planning (Fig.4b). Further spectral analysis on the trajectories revealed a 3-fold periodicity in travel length (Fig.4c, red arrow; $p < 0.05$, corrected for multiple comparisons), thereby confirming the prediction that the anisotropic pattern of the vector field leads to a similar anisotropic performance in path integration.

To validate whether the computational model described above successfully elucidate the mechanism underlying the emergence of the 3-fold periodicity observed in the human HPC, we would expect a similar periodical pattern in participants' behavioral performance. This is predicated on the notion that these low-frequency neural oscillations could propagate to higher-order regions such as the precuneus and the lateral parietal cortex, subsequently influencing participants' visuospatial judgement (Fig.4d). To test this prediction, we assessed participants' behavioral performance on the object-matching task in individual trials by integrating two metrics into a composite index: the travel length and the discrepancy between the intended goal location and the achieved endpoint (i.e., error size, see method for details). Shorter travel distances and smaller error magnitudes indicated better performance. A visual inspection of participants' behavioral data, sorted by global direction, showed a distinct 3-fold periodicity within the spatial domain (Fig. 4e). This behavioral periodicity was observable even at the individual level, where 16 out of 20 participants exhibited performance periodicity approximating 3Hz (Fig.S7).

Subsequent spectral analysis confirmed the significance of this behavioral periodicity, identifying a peak spectral power at a frequency of 3.36Hz (Fig.4f; $p < 0.05$, corrected for multiple comparisons). To further establish a causal relationship between HPC neural activity periodicity and behavioral performance, we examined the phase-locking coherence between them across participants. The mean Phase-Locking Value (PLV) was significantly higher than that in the shuffled control (Fig.4g; $p < 0.05$, corrected for multiple comparisons), suggesting a causal impact of HPC neural periodicity on behavioral periodicity at the spatial frequency of 3Hz. Taken together, the behavioral periodicity identified in human participants corroborates the model's prediction, thereby substantiating the model as a mechanistic framework for understanding the empirically observed vector field in the human HPC.

Discussion

The HPC and ERC of the brain perform distinct functions, the entorhinal grid cells construct the metric of space (Hafting et al., 2005), while the hippocampal place cells encode the locations of space (O'Keefe & Dostrovsky, 1971). However, how the ERC-HPC circuitry achieves path integration has remained a fundamental question in neuroscience. We found that the CA1 area of HPC exhibited a 3-fold modulation, which indicated a fluctuation of the BOLD activity series as a function of conceptual directions. Consistent with recent discovery of hippocampal vector field (Ormond and O'Keefe., 2022), our results predicted the periodic property of vector fields along conceptual direction. To explain the formation of this periodicity of HPC, we first ensured the significant coherence in BOLD activity series between the HPC and ERC, suggesting that the 3-fold modulation of HPC might be formed by the projection of entorhinal grid cell ensembles. Second, the "E-H PhaseSync" Model, built to simulate conceptual navigation, confirmed the periodicity of the HPC, which is modulated by the alignment of travelling direction in route planning and the spatial axes of grid cell. Interestingly, our model further predicted the periodic task performance that fluctuated as a function of conceptual directions. Finally, the task performance of human participants validated the model prediction by exhibiting a significant 3-fold behavior periodicity, which phase-locked to the BOLD activity series of the HPC. Taken together, our results highlighted the role of grid cell population in signal projection to the HPC, where place cells bind the conceptual directions into vector fields and guide spatial-visual perception during path integration.

Path integration, denoting the ability in accessing spatial knowledge from the last moment of updating to the current one in both physical (Wang and Spelke; Gallistel, 2017) and abstract space (Epstein et al., 2017; Behrens et al., 2018; Park et al., 2020), relies on the input of spatial vector specified by the upcoming location and direction. Our study reported the 3-fold periodicity of HPC, where the activity of HPC, that modulated by conceptual directions, converged to three robust vectors of global direction lying on the 2-dimensional conceptual space. This result built a bridge between the prediction of "grid cell to place cell" model (i.e., plane waves; Solstad et al., 2006; de Almeida et al., 2009; Bush et al., 2014; Bush et al., 2015; Bicanski and Burgess, 2019) and the phenomenon of the direction encoding of the HPC (McNaughton et al., 1983; Muller et al., 1994; Leutgeb et al., 2000; Rubin et al., 2014; Meister and Buffalo, 2016; Sarel et al., 2017; Ormond and O'Keefe., 2022). Under the framework of spatial imagining and planning, the plane

waves, generated by the "grid cell to place cell" model, are projected to place cells so that the direction-selective vector fields are formed. This explanation is consistent with previous finding of the oscillatory interference (Welday et al., 2011), the spatially periodic bands (Krupic et al., 2012), and the ConSinks (Ormond and O'Keefe., 2022) observed in the firing patterns of grid and place cells. Inspired by the phenomenon of behavior periodicity previously found in visual-target detection task (Fiebelkorn et al., 2011; Landau and Fries, 2012), and the capacity of grid and place cell in encoding visual space that beyond the scope of the MTL (Rubin et al., 2014; Julian et al., 2018; Staudigl et al., 2018), we examined the behavioral periodicity of human participants, and found the 3-fold representation of behavioral performance, which validated the propagation of neural activity in the ERC to the HPC and brain networks.

Controversies regarding the formation of place fields persist for decades, although our study support the "grid cell to place cell" model. Several earlier studies showed evidence that place fields are initially established in the absence of grid cell. For example, Wills et al (2010) recorded the neural activity of rat pups during foraging outside of the nest for the first time, the adultlike place cell activity emerged earlier at postnatal day 15 than that of stable grid cell activity presented at postnatal day 20 (see also Langston et al.,2010). Koenig et al (2011) diminished theta oscillations in the ERC-HPC circuitry by silencing the septal area such that the grid-like firing patterns of freely-moving rats were vanished, the place codes of location were nevertheless less affected despite a substantial decrease in firing rate. One of the possible explanations to this controversy might be the level of task demand. That is, those developmental studies typically arrange young animals to freely forage in open fields, where no demand of route planning was required. On the other hand, place fields might be also formed by visual cues (Bush et al., 2014). In spatial reorientation experiments, the disoriented mice in rectangular chamber often retrieve a reward by digging in the location that was diagonally opposite to the correct location. Meanwhile, the rate maps of place cells were formed aligning to geometric ambiguities (Keinath et al., 2017), suggesting that mice use the local geometry from visual inputs when the knowledge of allocentric map was not accessible (Gallistel, 2017; Julian et al., 2018). Those results reflect two distinct mechanisms of place field formation, the allocentric route planning dependent path integration and visual cue dependent path integration, in correspond to current controversies.

A limitation of our study is that the "E-H PhaseSync" model only provide explanation to the formation of hippocampal vector fields, which explain knowledge retrieval and decisions in

585 certain task demand. However, how the vector field promotes the update of the structured
586 knowledge coded by grid cells in context-specific scene, such as an unexpected landmark or an
587 obstacle, remains unsolved. ERC receives context and object information from the
588 parahippocampal cortex (PHC) and perirhinal cortex (PRC), respectively (Eichenbaum and Lipton,
589 2008; Montaldi and Mayes, 2010; Wilson et al., 2013). Further studies may build the framework
590 of MTL beyond the ERC-HPC circuitry (Rennó-Costa and Tort, 2017; Whittington et al., 2020)
591 and attempt to illustrate the self-organized capacity of biological brain during path integration.
592 One possibility is that the ERC extracts the projections from the PHC and PRC, and form the self-
593 or goal-location adapted reference frames (Stensola et al., 2015; Bottini and Doeller, 2020),
594 through the excitation-inhibition dynamics of grid cell ensembles (Amari, 1977; Samsonovich &
595 McNaughton, 1997; Fuhs & Touretzky, 2006; Burak & Fiete, 2009; Couey et al., 2013). Together,
596 the generality of MTL may reflect a hypothetic process of neuronal recycling (Dehaene and Cohen,
597 2007), in which the mapping of a variety of mental spaces that flexibly organized by ongoing
598 experiences would greatly help to explain the unified percept of the world efficiently (VanRullen
599 and Kanai, 2021).
600
601

Data availability

The data that support the findings of this study are available from the lead corresponding author (J.L.) upon request.

Code availability

All analyzes reported in this work were conducted with customized codes written in Python (version 3.9), Pygame (version 2.0), Matlab (version 2019b), R (version 4.0), and GNU bash (version 3.2.57). The codes will be available from the corresponding author (J.L.) upon request. The neuroimaging toolbox and machine learning framework used by the present work are publicly available as following: FreeSurfer (v7.1, https://surfer.nmr.mgh.harvard.edu/), FSL (version 6.0, https://fsl.fmrib.ox.ac.uk/fsl/fslwiki;), and Torch (version 1.9, https://pytorch.org/).

Acknowledgments

We gratefully acknowledge Mr. Yue Wu and Ms. Yuannan Li for the discussion on results and computational modelling, Dr. Michael Tarr for sharing the code for greeble stimulus generation. Computational work was supported by High-performance Computing Platform of Peking University. The work was supported by the National Key R&D Program of China (2020AAA0105200), China Postdoctoral Science Foundation (2022M710470), Beijing Municipal Science & Technology Commission & Administrative Commission of Zhongguancun Science Park (Z221100002722012), Tsinghua University Guoqiang Institute (2020GQG1016), and Beijing Academy of Artificial Intelligence (BAAI).

Conflict of interest

None declared

Author Contributions

J.L. conceived the study and provided advice. B.Z. conducted the fMRI study, performed the analysis, and built the computational model. B.Z. and J.L. wrote the paper.

Reference

Amari, S. (1977). Dynamics of pattern formation in lateral-inhibition type neural fields. Biol Cybern, 27(2), 77-87. https://doi.org/10.1007/BF00337259

Buzsaki, G. (2006). *Rhythms of the Brain*. Oxford university press.

Burgess, N., Barry, C., & O'Keefe, J. (2007). An oscillatory interference model of grid cell firing. Hippocampus, 17(9), 801-812. https://doi.org/10.1002/hipo.20327

Blair, H. T., Welday, A. C., & Zhang, K. (2007). Scale-invariant memory representations emerge from moire interference between grid fields that produce theta oscillations: a computational model. Journal of Neuroscience, 27(12), 3211-3229.

Burak, Y., & Fiete, I. R. (2009). Accurate path integration in continuous attractor network models of grid cells. PLoS Comput Biol, 5(2), e1000291. https://doi.org/10.1371/journal.pcbi.1000291

Buckner, R. L. (2010). The role of the hippocampus in prediction and imagination. *Annual review of psychology*, *61*, 27-48.

Bush, D., Barry, C., & Burgess, N. (2014). What do grid cells contribute to place cell firing? Trends Neurosci, 37(3), 136-145. https://doi.org/10.1016/j.tins.2013.12.003

Bieri, K. W., Bobbitt, K. N., & Colgin, L. L. (2014). Slow and fast gamma rhythms coordinate different spatial coding modes in hippocampal place cells. Neuron, 82(3), 670-681. https://doi.org/10.1016/j.neuron.2014.03.013

Bush, D., Barry, C., Manson, D., & Burgess, N. (2015). Using grid cells for navigation. Neuron, 87(3), 507-520. https://doi.org/10.1016/j.neuron.2015.07.006

Behrens, T. E., Muller, T. H., Whittington, J. C., Mark, S., Baram, A. B., Stachenfeld, K. L., & Kurth-Nelson, Z. (2018). What is a cognitive map? Organizing knowledge for flexible behavior. *Neuron*, *100*(2), 490-509.

Bao, X., Gjorgieva, E., Shanahan, L. K., Howard, J. D., Kahnt, T., & Gottfried, J. A. (2019). Grid-like Neural Representations Support Olfactory Navigation of a Two-Dimensional Odor Space. Neuron, 102(5), 1066-1075 e1065. https://doi.org/10.1016/j.neuron.2019.03.034

Bush, D., & Schmidt-Hieber, C. (2018). Computational models of grid cell firing. Hippocampal Microcircuits: A Computational Modeler's Resource Book, 585-613.

Bicanski, A., & Burgess, N. (2019). A computational model of visual recognition memory via grid cells. Current Biology, 29(6), 979-990.

Bottini, R., & Doeller, C. F. (2020). Knowledge across reference frames: Cognitive maps and image spaces. *Trends in Cognitive Sciences*, *24*(8), 606-619.

Canolty, R. T., Edwards, E., Dalal, S. S., Soltani, M., Nagarajan, S. S., Kirsch, H. E., ... & Knight, R. T. (2006). High gamma power is phase-locked to theta oscillations in human neocortex. *science*, *313*(5793), 1626-1628.

Colgin, L. L., Moser, E. I., & Moser, M. B. (2008). Understanding memory through hippocampal remapping. *Trends in neurosciences*, *31*(9), 469-477.

Couey, J. J., Witoelar, A., Zhang, S. J., Zheng, K., Ye, J., Dunn, B., Czajkowski, R., Moser, M. B., Moser, E. I., Roudi, Y., & Witter, M. P. (2013). Recurrent inhibitory circuitry as a mechanism for grid formation. Nat Neurosci, 16(3), 318-324. https://doi.org/10.1038/nn.3310

Constantinescu, A. O., O'Reilly, J. X., & Behrens, T. E. J. (2016). Organizing conceptual knowledge in humans with a gridlike code. Science, 352(6292), 1464-1468. https://doi.org/10.1126/science.aaf0941

De Valois, R. L., Albrecht, D. G., & Thorell, L. G. (1982). Spatial frequency selectivity of cells in macaque visual cortex. Vision Res, 22(5), 545-559. https://doi.org/10.1016/0042-6989(82)90113-4

Diba, K., & Buzsáki, G. (2007). Forward and reverse hippocampal place-cell sequences during ripples. *Nature neuroscience*, *10*(10), 1241-1242.

Dehaene, S., & Cohen, L. (2007). Cultural recycling of cortical maps. Neuron, 56(2), 384-398. https://doi.org/10.1016/j.neuron.2007.10.004

de Almeida, L., Idiart, M., & Lisman, J. E. (2009). The input–output transformation of the hippocampal granule cells: from grid cells to place fields. *Journal of Neuroscience*, *29*(23), 7504-7512.

Doeller, C. F., Barry, C., & Burgess, N. (2010). Evidence for grid cells in a human memory network. Nature, 463(7281), 657-661. https://doi.org/10.1038/nature08704

Dragoi, G., & Tonegawa, S. (2011). Preplay of future place cell sequences by hippocampal cellular assemblies. *Nature*, *469*(7330), 397-401.

Eichenbaum, H., & Lipton, P. A. (2008). Towards a functional organization of the medial temporal lobe memory system: role of the parahippocampal and medial entorhinal cortical areas. *Hippocampus*, *18*(12), 1314-1324.

Epstein, R. A., Patai, E. Z., Julian, J. B., & Spiers, H. J. (2017). The cognitive map in humans: spatial navigation and beyond. *Nature neuroscience*, *20*(11), 1504-1513.

Fyhn, M., Hafting, T., Treves, A., Moser, M. B., & Moser, E. I. (2007). Hippocampal remapping and grid realignment in entorhinal cortex. *Nature*, *446*(7132), 190-194.

Fyhn, M., Hafting, T., Witter, M. P., Moser, E. I., & Moser, M. B. (2008). Grid cells in mice. Hippocampus, 18(12), 1230-1238. https://doi.org/10.1002/hipo.20472

Fiebelkorn, I. C., Pinsk, M. A., & Kastner, S. (2018). A Dynamic Interplay within the Frontoparietal Network Underlies Rhythmic Spatial Attention. Neuron, 99(4), 842-853 e848. https://doi.org/10.1016/j.neuron.2018.07.038

Fuhs, M. C., & Touretzky, D. S. (2006). A spin glass model of path integration in rat medial entorhinal cortex. Journal of Neuroscience, 26(16), 4266-4276.

Gauthier, I., & Tarr, M. J. (1997). Becoming a "Greeble" expert: exploring mechanisms for face recognition. Vision Res, 37(12), 1673-1682. https://doi.org/10.1016/s0042-6989(96)00286-6

Guanella, A., Kiper, D., & Verschure, P. (2007). A model of grid cells based on a twisted torus topology. Int J Neural Syst, 17(4), 231-240. https://doi.org/10.1142/S0129065707001093

Gallistel, C. R. (2017). Navigation: whence our sense of direction?. *Current Biology*, *27*(3), R108-R110.

Gerlei, K., Passlack, J., Hawes, I., Vandrey, B., Stevens, H., Papastathopoulos, I., & Nolan, M. F. (2020). Grid cells are modulated by local head direction. Nature communications, 11(1), 4228.

Garcia, A. D., & Buffalo, E. A. (2020). Anatomy and function of the primate entorhinal cortex. *Annual Review of Vision Science*, *6*, 411-432.

Gardner, R. J., Hermansen, E., Pachitariu, M., Burak, Y., Baas, N. A., Dunn, B. A., ... & Moser, E. I. (2022). Toroidal topology of population activity in grid cells. *Nature*, *602*(7895), 123-128.

Hubel, D. H., & Wiesel, T. N. (1959). Receptive fields of single neurones in the cat's striate cortex. J Physiol, 148, 574-591. https://doi.org/10.1113/jphysiol.1959.sp006308

Hubel, D. H., & Wiesel, T. N. (1962). Receptive fields, binocular interaction and functional architecture in the cat's visual cortex. J Physiol, 160, 106-154. https://doi.org/10.1113/jphysiol.1962.sp006837

Hafting, T., Fyhn, M., Molden, S., Moser, M. B., & Moser, E. I. (2005). Microstructure of a spatial map in the entorhinal cortex. Nature, 436(7052), 801-806. https://doi.org/10.1038/nature03721

Hales, J. B., Schlesiger, M. I., Leutgeb, J. K., Squire, L. R., Leutgeb, S., & Clark, R. E. (2014). Medial entorhinal cortex lesions only partially disrupt hippocampal place cells and hippocampus-dependent place memory. *Cell reports*, *9*(3), 893-901.

Insausti, R., Juottonen, K., Soininen, H., Insausti, A. M., Partanen, K., Vainio, P., Laakso, M. P., & Pitkanen, A. (1998). MR volumetric analysis of the human entorhinal, perirhinal, and temporopolar cortices. AJNR Am J Neuroradiol, 19(4), 659-671. https://www.ncbi.nlm.nih.gov/pubmed/9576651

Iglesias, J. E., Augustinack, J. C., Nguyen, K., Player, C. M., Player, A., Wright, M., Roy, N., Frosch, M. P., McKee, A. C., Wald, L. L., Fischl, B., Van Leemput, K., & Alzheimer's Disease Neuroimaging, I. (2015). A computational atlas of the hippocampal formation using ex vivo, ultra-high resolution MRI: Application to adaptive segmentation of in vivo MRI. Neuroimage, 115, 117-137. https://doi.org/10.1016/j.neuroimage.2015.04.042

Jenkinson, M., & Smith, S. (2001). A global optimisation method for robust affine registration of brain images. Med Image Anal, 5(2), 143-156. https://doi.org/10.1016/s1361-8415(01)00036-6

Johnson, A., Seeland, K., & Redish, A. D. (2005). Reconstruction of the postsubiculum head direction signal from neural ensembles. Hippocampus, 15(1), 86-96.

Jeffery, K. J. (2007). Integration of the sensory inputs to place cells: what, where, why, and how?. *Hippocampus*, *17*(9), 775-785.

Jeffery, K. J., Page, H. J., & Stringer, S. M. (2016). Optimal cue combination and landmark-stability learning in the head direction system. *The Journal of physiology*, *594*(22), 6527-6534.

Julian, J. B., Keinath, A. T., Marchette, S. A., & Epstein, R. A. (2018). The neurocognitive basis of spatial reorientation. *Current Biology*, *28*(17), R1059-R1073.

Koenig, J., Linder, A. N., Leutgeb, J. K., & Leutgeb, S. (2011). The spatial periodicity of grid cells is not sustained during reduced theta oscillations. *Science*, *332*(6029), 592-595.

Krupic, J., Burgess, N., & O'Keefe, J. (2012). Neural representations of location composed of spatially periodic bands. Science, 337(6096), 853-857. https://doi.org/10.1126/science.1222403

Killian, N. J., Jutras, M. J., & Buffalo, E. A. (2012). A map of visual space in the primate entorhinal cortex. Nature, 491(7426), 761-764. https://doi.org/10.1038/nature11587

Krupic, J., Bauza, M., Burton, S., Barry, C., & O'Keefe, J. (2015). Grid cell symmetry is shaped by environmental geometry. *Nature*, *518*(7538), 232-235.

Keinath, A. T., Julian, J. B., Epstein, R. A., & Muzzio, I. A. (2017). Environmental geometry aligns the hippocampal map during spatial reorientation. *Current Biology*, *27*(3), 309-317.

Kang, L., & Balasubramanian, V. (2019). A geometric attractor mechanism for self-organization of entorhinal grid modules. Elife, 8, e46687.

Landau, A. N., & Fries, P. (2012). Attention samples stimuli rhythmically. Curr Biol, 22(11), 1000-1004. https://doi.org/10.1016/j.cub.2012.03.054

Leutgeb, S., Ragozzino, K. E., & Mizumori, S. J. (2000). Convergence of head direction and place information in the CA1 region of hippocampus. Neuroscience, 100(1), 11-19.

Langston, R. F., Ainge, J. A., Couey, J. J., Canto, C. B., Bjerknes, T. L., Witter, M. P., ... & Moser, M. B. (2010). Development of the spatial representation system in the rat. *Science*, *328*(5985), 1576-1580.

Lisman, J., Buzsáki, G., Eichenbaum, H., Nadel, L., Ranganath, C., & Redish, A. D. (2017). Viewpoints: how the hippocampus contributes to memory, navigation and cognition. Nature neuroscience, 20(11), 1434-1447.

McNaughton, B. L., Barnes, C. A., & O'Keefe, J. J. E. B. R. (1983). The contributions of position, direction, and velocity to single unit activity in the hippocampus of freely-moving rats. *Experimental brain research*, *52*, 41-49.

Muller, R. U., Bostock, E., Taube, J. S., & Kubie, J. L. (1994). On the directional firing properties of hippocampal place cells. *Journal of Neuroscience*, *14*(12), 7235-7251.

Montaldi, D., & Mayes, A. R. (2010). The role of recollection and familiarity in the functional differentiation of the medial temporal lobes. *Hippocampus*, *20*(11), 1291-1314.

Mullally, S. L., & Maguire, E. A. (2014). Memory, imagination, and predicting the future: A common brain mechanism?. *The Neuroscientist*, *20*(3), 220-234.

Meister, M. L., & Buffalo, E. A. (2016). Getting directions from the hippocampus: The neural connection between looking and memory. *Neurobiology of learning and memory*, *134*, 135-144.

McNamee, D. C., Stachenfeld, K. L., Botvinick, M. M., & Gershman, S. J. (2021). Flexible modulation of sequence generation in the entorhinal-hippocampal system. Nat Neurosci, 24(6), 851-862. https://doi.org/10.1038/s41593-021-00831-7

Nichols, T. E., & Holmes, A. P. (2002). Nonparametric permutation tests for functional neuroimaging: a primer with examples. Hum Brain Mapp, 15(1), 1-25. https://doi.org/10.1002/hbm.1058

Nau, M., Navarro Schroder, T., Bellmund, J. L. S., & Doeller, C. F. (2018). Hexadirectional coding of visual space in human entorhinal cortex. Nat Neurosci, 21(2), 188-190. https://doi.org/10.1038/s41593-017-0050-8

Nyberg, N., Duvelle, É., Barry, C., & Spiers, H. J. (2022). Spatial goal coding in the hippocampal formation. Neuron.

O'Keefe, J., & Dostrovsky, J. (1971). The hippocampus as a spatial map: preliminary evidence from unit activity in the freely-moving rat. Brain research. https://doi.org/10.1016/0006-8993(71)90358-1

O'keefe, J., & Burgess, N. (2005). Dual phase and rate coding in hippocampal place cells: theoretical significance and relationship to entorhinal grid cells. Hippocampus, 15(7), 853-866.

Ormond, J., & O'Keefe, J. (2022). Hippocampal place cells have goal-oriented vector fields during navigation. Nature, 607(7920), 741-746.

Park, S. A., Miller, D. S., Nili, H., Ranganath, C., & Boorman, E. D. (2020). Map making: constructing, combining, and inferring on abstract cognitive maps. *Neuron*, *107*(6), 1226-1238.

Pfeiffer, B. E. (2020). The content of hippocampal "replay". *Hippocampus*, *30*(1), 6-18.

Rubin, A., Yartsev, M. M., & Ulanovsky, N. (2014). Encoding of head direction by hippocampal place cells in bats. *Journal of Neuroscience*, *34*(3), 1067-1080.

Rennó-Costa, C., & Tort, A. B. (2017). Place and grid cells in a loop: implications for memory function and spatial coding. *Journal of Neuroscience*, *37*(34), 8062-8076.

Samsonovich, A., & McNaughton, B. L. (1997). Path integration and cognitive mapping in a continuous attractor neural network model. J Neurosci, 17(15), 5900-5920. https://www.ncbi.nlm.nih.gov/pubmed/9221787

Solstad, T., Moser, E. I., & Einevoll, G. T. (2006). From grid cells to place cells: a mathematical model. Hippocampus, 16(12), 1026-1031. https://doi.org/10.1002/hipo.20244

Stam, C. J., Nolte, G., & Daffertshofer, A. (2007). Phase lag index: assessment of functional connectivity from multi channel EEG and MEG with diminished bias from common sources. *Human brain mapping*, *28*(11), 1178-1193.

Sullivan, G.M., Feinn, R., 2012. Using effect size—Or why the P value is not enough. J.Grad. Med. Educ. 4 (3), 279–282. doi:10.4300/JGME-D-12-00156.1.

Stemmler, M., Mathis, A., & Herz, A. V. (2015). Connecting multiple spatial scales to decode the population activity of grid cells. Sci Adv, 1(11), e1500816. https://doi.org/10.1126/science.1500816

Schlichting, M. L., Mumford, J. A., & Preston, A. R. (2015). Learning-related representational changes reveal dissociable integration and separation signatures in the hippocampus and prefrontal cortex. Nat Commun, 6, 8151. https://doi.org/10.1038/ncomms9151

Stensola, T., Stensola, H., Moser, M. B., & Moser, E. I. (2015). Shearing-induced asymmetry in entorhinal grid cells. *Nature*, *518*(7538), 207-212.

Sarel, A., Finkelstein, A., Las, L., & Ulanovsky, N. (2017). Vectorial representation of spatial goals in the hippocampus of bats. *Science*, *355*(6321), 176-180.

Sosa, M., & Giocomo, L. M. (2021). Navigating for reward. Nat Rev Neurosci, 22(8), 472-487. https://doi.org/10.1038/s41583-021-00479-z

Tolman, E. C. (1948). Cognitive maps in rats and men. Psychol Rev, 55(4), 189-208. https://doi.org/10.1037/h0061626

Taube, J. S., Muller, R. U., & Ranck, J. B. (1990). Head-direction cells recorded from the postsubiculum in freely moving rats. I. Description and quantitative analysis. Journal of Neuroscience, 10(2), 420-435.

Taube, J. S. (2007). The head direction signal: origins and sensory-motor integration. Annu. Rev. Neurosci., 30, 181-207.

Towers, Mark, Terry, Jordan K, Kwiatkowski, Ariel, Balis, John U., Cola, Gianluca, Deleu, Tristan, Goulão, Manuel, Kallinteris, Andreas, KG, Arjun, Krimmel, Markus, Perez-Vicente, Rodrigo, Pierré, Andrea, Schulhoff, Sander, Tai, Jun Jet, Tan, Andrew Jin Shen, & Younis, Omar G. (2023). Gymnasium (v0.29.0). Zenodo. https://doi.org/10.5281/zenodo.8148697

van Groen, T., Miettinen, P., & Kadish, I. (2003). The entorhinal cortex of the mouse: organization of the projection to the hippocampal formation. Hippocampus, 13(1), 133-149. https://doi.org/10.1002/hipo.10037

VanRullen, R., & Kanai, R. (2021). Deep learning and the Global Workspace Theory. Trends Neurosci, 44(9), 692-704. https://doi.org/10.1016/j.tins.2021.04.005

Witter, M. P., & Amaral, D. G. (1991). Entorhinal cortex of the monkey: V. Projections to the dentate gyrus, hippocampus, and subicular complex. J Comp Neurol, 307(3), 437-459. https://doi.org/10.1002/cne.903070308

Woolrich, M. W., Ripley, B. D., Brady, M., & Smith, S. M. (2001). Temporal autocorrelation in univariate linear modeling of FMRI data. Neuroimage, 14(6), 1370-1386. https://doi.org/10.1006/nimg.2001.0931

Wang, R. F., & Spelke, E. S. (2002). Human spatial representation: Insights from animals. *Trends in cognitive sciences*, *6*(9), 376-382.

Woolrich, M. W., Behrens, T. E., & Smith, S. M. (2004). Constrained linear basis sets for HRF modelling using Variational Bayes. Neuroimage, 21(4), 1748-1761. https://doi.org/10.1016/j.neuroimage.2003.12.024

Wills, T. J., Cacucci, F., Burgess, N., & O'Keefe, J. (2010). Development of the hippocampal cognitive map in preweanling rats. *science*, *328*(5985), 1573-1576.

Winter, S. S., & Taube, J. S. (2014). Head direction cells: from generation to integration. In Space, time and memory in the hippocampal formation (pp. 83-106). Vienna: Springer Vienna.

Welday, A. C., Shlifer, I. G., Bloom, M. L., Zhang, K., & Blair, H. T. (2011). Cosine directional tuning of theta cell burst frequencies: evidence for spatial coding by oscillatory interference. *Journal of Neuroscience*, *31*(45), 16157-16176.

Wilson, D. I., Langston, R. F., Schlesiger, M. I., Wagner, M., Watanabe, S., & Ainge, J. A. (2013). Lateral entorhinal cortex is critical for novel object-context recognition. *Hippocampus*, *23*(5), 352-366.

Whittington, J. C., Muller, T. H., Mark, S., Chen, G., Barry, C., Burgess, N., & Behrens, T. E. (2020). The Tolman-Eichenbaum machine: unifying space and relational memory through generalization in the hippocampal formation. *Cell*, *183*(5), 1249-1263.

Whittington, J. C., McCaffary, D., Bakermans, J. J., & Behrens, T. E. (2022). How to build a cognitive map. *Nature neuroscience*, *25*(10), 1257-1272.

Methods

Participants

Two groups of right-handed university students with normal or corrected-to-normal vision were recruited. The first group, served as the experimental group, was 10 students from Peking University, and the second group contained ten students from Tsinghua University for replication purpose. Participants' age and sex were balanced between groups (experimental group: mean age = 22.10 [SD = 2.23], 5 females, 5 males; replication group: mean age = 23.9 [SD = 3.51], 5 females, 5 males). All participants had no history of psychiatric or neurological disorders and gave their written informed consent prior to the experiment, which was approved by the Research Ethics Committee of both universities.

Experimental design

Artificial object space. The greebles (Gauthier and Tarr, 1997) were created by 3ds Max (Autodesk, version 2022, http://www.autodesk.com) and the MAXScript codes from an open-source repository (TarrLab stimulus datasets, http://www.tarrlab.org/). The identity of individual greeble was determined by the lengths of its two components, named as "Loogit" and "Vacso" (Fig.1a, top). The names were arbitrary and had no relation to the object matching task (see below). We created 2025 greebles in total, each of which was equipped with a unique combination of Loogit's and Vacso's lengths. In this way, a 45-by-45 greeble space was constructed, with y-axis denoting Loogit's length and x-axis for Vacso's length (Fig. 1b). Therefore, in this 2-D artificial object space, each greeble represented a location. The greeble in the center of the space had equal length of Loogit and Vacso (i.e., prototype), which served as the target of the task. The ratio of a greeble parts' length over that of the prototype ranged from 0.12 to 1.88 with a step size of 0.04, which offered a smooth morphing experience when participants adjusted the length of object components.

Experimental procedure. In a trial of the object matching task, a greeble variant that was pseudo-randomly selected from greeble variants in the ring near the boundary of the space (red points in Fig.1b) was presented in the center of the screen after a 2.0-s fixation screen. The participants were instructed to adjust the lengths of the variant to match those of the prototype as quickly as possible by pressing buttons. There were four buttons, two of which were used to either stretching or shrinking one greeble part. When the participants felt that the adjusted variant completely matched

the prototype, they either pressed the return key to end the trial (self-pace in behavioral training) or waited the time limit to run out (fixed time limit in fMRI scan) (see below). To ensure paths from variants to the prototype covered most of locations in the space, 24 variants were randomly selected with its angular precision of 1° in each 30° bin of the ring, which made up 288 variants evenly distributed in the ring. The accuracy of a trial was indexed by the distance between prototype's location and the location where the participant stopped. To encourage the participants to perform the task as accurately as possible, participants were informed that the amount of their monetary compensation increased exponentially with their performance. The task was programmed by Python (version 3.9) and Pygame (a library designed for writing video games, version 2.0, https://www.pygame.org/).

The task was conducted twice in two consecutive days, one for behavioral training and the other for fMRI scan. In day 1, the participants adjusted the length of variant's parts to match the prototype in a self-paced fashion. There were 8 sessions with 36 trials each, which made up 288 trials in total and took about 1 hour. The first 7 sessions provided feedback at the end of trials (e.g., "Loogit: 5 percent longer than the target") and the 8th session had no feedback for measuring behavioral performance. Before the training, the participants learned the prototype by watching it on the screen, and then performed at least 10 trials with feedback as practice. In day 2, the procedure was identical to that of day 1, except that (1) the self-pace was replaced with a 10-s time limit for each trial with a timer presented on top of screen (Fig.1b), (2) no feedback was provided for all sessions, and (3) the participants finished the experiment in fMRI scanner. After the fMRI scan, the participants were debriefed, and none was aware of the existence of the object space or the analogy of the adjustment of the length of object components during path integration. The behavioral performance of participants that fluctuates as a function of conceptual directions was defined by $0.04 \times T + E$, where T represents the length of trajectory, denoting the movement steps, which was scaled into the distance of object space by a constant parameter 0.04, E denotes the error, quantified by the distance between the goal location and the location participants stopped in object space.

fMRI data acquisition

1028 Imaging data were collected using a 3T Siemens Prisma scanner equipped with a 64- and 20-
1029 channel receiver head coil for the experimental group and replication group at PKU and Tsinghua
1030 Imaging Center, respectively. Functional data were acquired with a Multi-band Echo Planer
1031 imaging (EPI) sequence (TR = 2000 ms, TE = 30 ms, matrix size: 112 × 112 x 62, flip angle: 90°,
1032 resolution: 2 × 2 × 2.3 mm^3, number of slices: 62, slice thickness: 2 mm, gap = 0.3 mm, slice
1033 orientation: transversal). A high-resolution T1-weighted three-dimensional anatomical data set
1034 was collected for registration (MPRAGE, TR = 2530 ms, TE = 2.98 ms, matrix size: 448 x 512 x
1035 192, flip angle: 7°, resolution: 0.5 × 0.5 × 1 mm3, number of slices: 192, slice thickness: 1 mm,
1036 slice orientation: sagittal). In the experimental group, stimuli were presented through a Sinorad
1037 LCD projector (Shenzhen Sinorad Medical Electronics) onto a 33-inch rear-projection screen. In
1038 the replication group, the stimuli were presented using a visual/audio stimulation system
1039 (Shenzhen Sinorad SA-9939) with a customized-design (Shenzhen Sinorad Medical Electronics
1040 Co., Ltd) MRI compatible 40" LED liquid crystal display. The resolution of screens was 1024 x
1041 768, and the participants viewed the stimuli with an angled mirror mounted on the head coil.
1042
1043 **fMRI data preprocessing**
1044 The BOLD signal time series of each scan session was preprocessed independently using FSL
1045 FEAT toolbox (FMRIB's Software Library, version 6.0, https://fsl.fmrib.ox.ac.uk/fsl/fslwiki;
1046 Woolrich et al. 2001; Woolrich et al. 2004). For each session, the time series were corrected for
1047 motion artefacts, slice time acquisition differences, geometrical distortion using the fieldmaps, and
1048 were high-pass filtered at 100 s. Spatial smoothing was further applied using a 5 mm FWHM
1049 Gaussian kernel. For group-level statistics, each session's functional data were registered to
1050 participant's high-resolution anatomical image and were then normalized to a standard image
1051 (MNI152) using FSL FLIRT (Jenkinson and Smith, 2001). This procedure also resampled the
1052 functional voxels into a 2 x 2 x 2 mm resolution.
1053
1054 **Sinusoid analysis**
1055 To test whether the hexagonal pattern was present during the object matching task, we first
1056 computed the hexagonal orientation in the ERC for each participant using one half of the data
1057 (odd-numbered sessions). Second, we looked for the hexagonal pattern that modulated by

1058 participants' spatial orientation ranging from 0° to 360° in the object space after controlling for
1059 the effect of the hexagonal orientation (Doeller et al., 2010; Constantinescu et al., 2016).
1060 Specifically, a GLM was created for each session to model the time series convolved with FSL
1061 Double-Gamma hemodynamic response function in the ERC with two parametric modulators:
1062 sin(6θ) and cos(6θ), where θ represents the spatial-orientation in the object space. The factor 6
1063 means the 6-folded neural activity, which is rotational symmetric and aligned with spatial-
1064 orientation. The factor 5 and 7 were used as controls, which misaligned with the hexagonal pattern.
1065 Those estimated parameters β_{sine} and β_{cosine} were subsequently used to compute the hexagonal
1066 orientation φ, ranged from 0° to 59°, in each voxel and each participant, where $\varphi =$
1067 $[\arctan(\frac{\beta_{sine}}{\beta_{cosine}})]/6$. The hexagonal orientation Φ for each participant was derived by averaging
1068 the φ map across the odd-numbered sessions and voxels in the ERC. Once the hexagonal pattern
1069 of neural activity in the ERC was identified, a second GLM was fitted to model the BOLD signals
1070 from the other half of the data (even-numbered sessions), which was specified by a cosine
1071 parametric modulator: cos(6[θ - Φ]). The activity map of the hexagonal pattern was derived by
1072 averaging the parametric map of this cosine modulator across the even-numbered sessions, which
1073 was further converted to z-score map before submitting to second-level analysis (Schlichting et al.,
1074 2015).
1075
1076 **Spectral analysis of MRI BOLD signals**
1077 To examine the spectrum of BOLD signals within the MTL, we created a GLM to extract the
1078 activity map corresponding to each spatial direction in the object space, and then performed voxel-
1079 based spectral analyses to identify robust periodic activity. Specifically, the spatial directions,
1080 which were represented by the trajectories from variants to the prototype, were first down-sampled
1081 into bins with 15° each (e.g., the spatial directions within -7.5° to 7.5°was label as 0° and the
1082 spatial directions within 337.5° to 352.5°was label as 345°). This procedure resulted in a vector of
1083 24 resampled spatial directions (i.e., the number of bins), which was sufficient samples for spectral
1084 analysis (De Valois et al., 1982) and was used to look for the spatial periodicity of neural activity
1085 ranged from 0Hz to 11Hz. Next, the BOLD signals in correspond to the spatial directions was
1086 modelled by a GLM with the directional bins specified as parametric modulators, producing the
1087 spatial direction-dependent activity maps for each participant, which were extracted from each
1088 voxel of the MTL, and were sorted in ascending order (i.e., 0° to 345°).

Next, we performed the spectral analysis on the BOLD activity series using the Fast Discrete Fourier Transform (FFT) included by the stats package of R platform (version 4.0, https://www.r-project.org/; Landau and Fries, 2012), where the detrending, Hanning tapper, and zero-padding were applied for preprocessing. The BOLD activity series was then converted into frequency domain from spatial domain, and the spectrum magnitude was derived by computing the absolute values of the complex FFT output. This procedure generated a brain map of magnitude for each frequency. The 95th percentile of pseudo t-statistic distribution (the mean magnitude divided by the SE across participants) was computed as the initial threshold for each voxel of the MTL for second-level analysis.

Anatomical masks

We manually delineated the bilateral ERC for ROI analyses on the MNI T1 brain with 2 mm resolution packaged by FSL using established protocols (Insausti et al. 1998), as well as a delineating software ITK-SNAP (Version 3.8, www.itksnap.org). The masks of HPC subfields were derived by an automated segmentation tool packaged by Freesurfer (Version 7.1, https://surfer.nmr.mgh.harvard.edu/; Iglesias et al., 2015), which segments the CA1 and CA2/3 area from hippocampal formation and further divides the mask into head and body parts. All masks were resampled to 2 mm resolution and aligned in standard MNI space.

The "R-H PhaseSync" model

The model, implemented using Torch (Version 1.13, Python version 3.9), was built to elucidate the algorithm behind the 3-fold periodicity observed in the HPC. The agent was arranged to perform path integration on a 45-by-45-pixel space, where each arbitrary spatial location (1 out of 2025 pixels) was denoted by the coordinate vector $r = (x, y)$. The process of path integration conforms with the winner-take-all dynamics (Bicanski & Burgess, 2019). Specifically, each ongoing location the agent moved toward was selected after looking for the surrounding locations with the strongest activity of place cells (Ormond & O'Keefe, 2022), where the place cell activities that code the locations over the space are assumed as the projection of grid cell ensembles. The agent moved following neural activity dynamics until the goal is approached.

Simulation of Entorhinal Grid cell. According to the moiré patterns proposal for hexagonal pattern formation (O'keefe and Burgess, 2005; Burgess et al., 2007; Blair et al., 2007; Bush and Schmidt-Hieber, 2018), grid cells were generated by the cosine grating model. For single cell, the spatial code G at spatial location $r_{(x,y)}$ was derived by summing three cosine gratings under the spatial phase $c_{(x_0,y_0)}$(Equation 3). The cosine gratings were oriented by the rotation vector k with 60° apart from one another. A denotes the amplitude of cosine gratings. Four spatial codes of grid cell, each denoted by grid module Ω, were generated for each spatial location $r_{(x,y)}$ to acheive multi-scale encoding. The scale-ratio of approximately 1.4 was used according to the suggestion from previous simulations (Kang and Balasubramanian, 2019; Killian et al., 2012; Stemmler et al., 2015). A total of 2024 grid cells were finally generated in each grid module, where grid orientations were consistent, while grid phases were varied.

$$G_r = \sum_{i=1}^{3} A\cos(\omega_i(k_{i,x}(r_x - c_x) + k_{i,y}(r_y - c_y))) \tag{3}$$

Simulation of Hippocampal vector field. HPC has the capacity of encoding both direction and location (McNaughton et al., 1983; Muller et al., 1994; Rubin et al., 2014; Meister and Buffalo, 2016), which form the vector representation of space to drive path integration (Leutgeb et al., 2000; Sarel et al., 2017; Ormond and O'Keefe., 2022). To model this capacity, we hypothesized that the hippocampal vector field C_r over two-dimensional space is the integration of the place cell ensembles of $C_{Direction_r}$, which encodes direction-selective activity, and $C_{Location_r}$ that encodes location-selective activity, respectively (Equation 2). Each of $C_{Location_r}$ and $C_{Direction_r}$ specifies a two-dimensional matrix averaged across Ω. The rationale behind the hypothesis was based on the functional separation of ERC and HPC. The spatial periodicity of ERC, which has been known to encode directions (Doeller et al., 2010; Constantinescu et al., 2016; Bao et al., 2019), might be projected to HPC via ERC-HPC circuit (Fyhn et al., 2007; Hales et al., 2014), while the prospective encoding of locations has been known as the internal representation of the HPC (Bush et al., 2015; Sarel et al., 2017; Nyberg et al., 2022).

$C_{Direction_r}$ is defined by the size of angle difference δ_r between the head-direction ϕ_r, which was reconstructed from the conjunctive grid codes V_{ψ,r_i} projected from post-subiculum (Equation 1; Taube et al., 1990; Taube, 2007; Fyhn et al., 2008; Winter and Taube, 2014; Gerlei et al., 2020), and the global direction ψ_r. To derive ϕ_r, V_{ψ,r_i} is generated for each location r via the linear combinations of grid codes activated by imagining and planning (Fig.3a & b, Lisman et al., 2017; Whittington et al., 2022). The activity vector f, which specifies the preferences of direction, was constructed from V_{ψ,r_i} (Johnson et al., 2005), then the preferred direction ϕ_r can be derived from the maxima of standardized f using the find_peaks function (Scipy, version 1.9.3).

$$\phi_r = \begin{cases} \arg\max_\psi \mathcal{Z}\{\sum_n V_{\psi,r_n}\} & \text{if } m \geq 1 \text{ and } (\Lambda_m - \Lambda_{m-1}) > 2\sigma \\ (\psi_r + \frac{\pi}{2})\%\pi & \text{otherwise} \end{cases} \tag{4}$$

The noises of ϕ_r are typically characterized by the multiple-peak (i.e., $m > 1$) pattern identified in vector f particularly in the travels where the head directions misaligned with primary grid axes, to simplify the simulation, we thresholded $\emptyset$ by 2σ of the vector of peak amplitudes Λ, where the amplitudes were sorted in ascending order (Equation 4). In other words, ϕ_r that not exceeding the 2σ of Λ is assigned with a direction perpendicular to ψ_r, resulting in a constant $\emptyset$ for the purpose of noise reduction.

$$C_{\text{Direction}r} = \begin{cases} \pi - \delta_r & \text{if } \delta < \frac{\pi}{2} \\ \delta_r & \text{otherwise} \end{cases} \tag{5}$$

At each potential location of travelling, the head-direction ϕ_r was compared with the global direction of the location, resulting the angle difference δ_r. The smaller value of δ_r corresponds to the higher level of place cell activity. Next, δ_r was linearly transformed into winner-take-all dynamics before filling the location of direction map $C_{Direction}$ (Equation 5). $C_{Location}$, which is insensitive to spatial directions but encode the distance with the goal-location, is simulated by a Q-value map by training a standard RL model over the two-dimensional space using Gymnasium library (OpenAI, version=0.29; Towers et al., 2023).

In navigational simulation, a total of 156 locations, forming a ring-shaped pattern near the boundary of space, serve as the starting locations. This configuration resulted in a set of global directions ranged from 0° to 360° relative to the goal in the center (yellow points in Fig.1c &

orange points in Fig.4a). In each travel step, a vector of place cell activity that encodes the locations surrounded by self-location was extracted from C, the agent moved to the location with the strongest place cell activity to approach one transition. During this process, the step size was adapted to a stepwise approach. That is, an initial step size of 1 pixel was assigned to the movement, and it was increased by 1 pixel if no stronger activity was found from the surrounding locations until the next location was localized. The sequences of coordinates between the starting- and goal-location were recorded in each trial, the travel length was computed by the sum of the distances of every location-pairs. The vector of travel lengths across trials were then sorted by global directions with ascending order before submitting to spectrum analysis.

Statistical analysis

The 3-fold and 6-fold neural periodicity were examined by cluster-based permutation using FSL randomise package (version 2.9, http://fsl.fmrib.ox.ac.uk/fsl/fslwiki/Randomise), where an initial threshold of $p < 0.01$ was used to derive the uncorrected clusters. If no clusters were revealed, a liberal threshold of $p < 0.05$ was used. The reliability of the uncorrected clusters was further tested using a non-parametric statistical inference that does not make assumptions about the distribution of the data (Nichols and Holmes 2002). Specifically, 1,000 random sign-flips were performed on the beta or FFT magnitude images. The clusters with size higher than 95% of the maximal suprathreshold clusters from permutation distribution were reported. The periodicity of behavioral performance recorded from human participants and the "E-H PhaseSync" model was examined using FFT, where the initial threshold of each frequency was derived from the 95% percentile of shuffled magnitude distribution, the threshold corrected for multiple comparison was selected by the maximum of the initial thresholds across frequencies. The coherence between the BOLD activity series of the ERC and HPC and between the BOLD activity series of HPC and task performance series in conceptual directions was examined using the amplitude-phase coupling analysis (Canolty et al., 2006) and the phase-lag index analysis (Stam et al., 2007), respectively. Note that no band-passed filter was applied to either the ERC or HPC BOLD signal series. The robustness of coherence was evaluated by permutation test with 1000 shuffling applied on the conceptual directions. The coherence that higher than the top 5% of shuffled distribution was considered to be significant. All the t-tests used in the present study were two-tailed.

Supplemental Material

"Population activities of grid cells predict hippocampal and behavior periodicity during path integration"

Bo Zhang and Jia Liu

Figure S1. Behavioral results of the human participants from the experimental and replication group. The error was defined as the distance between the prototype location and the location where the participants stopped. In day 1, the task errors decreased as a function of experimental sessions, resulting a significantly negative slope for both groups of participants (experimental group: $t(9) = -3.90$, $p = 0.003$; replication group: $t(9) = -2.82$, $p = 0.019$). No significant learning effect was found during the MRI scan of day 2 (experimental group: $t(9) = -0.22$, $p = 0.834$; replication group: $t(9) = -0.10$, $p = 0.922$). This design ruled out the possibility of learning effect in examining the neural periodicity within the MTL. Error bars indicate SEM.

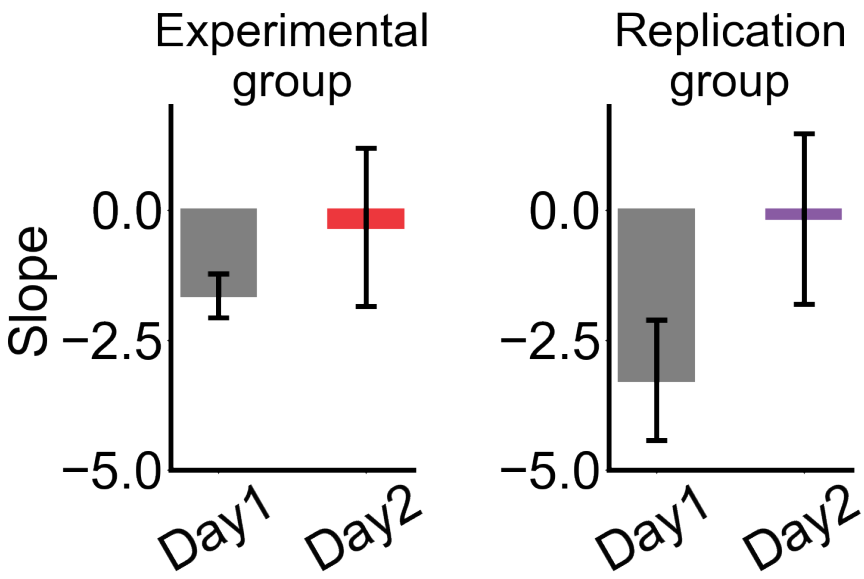

Figure S2. Trajectories of human participants recorded during MRI scanning. The orange dots denote the start locations while the red/purple dots indicate the end locations for the experimental (red) and replication (purple) group.

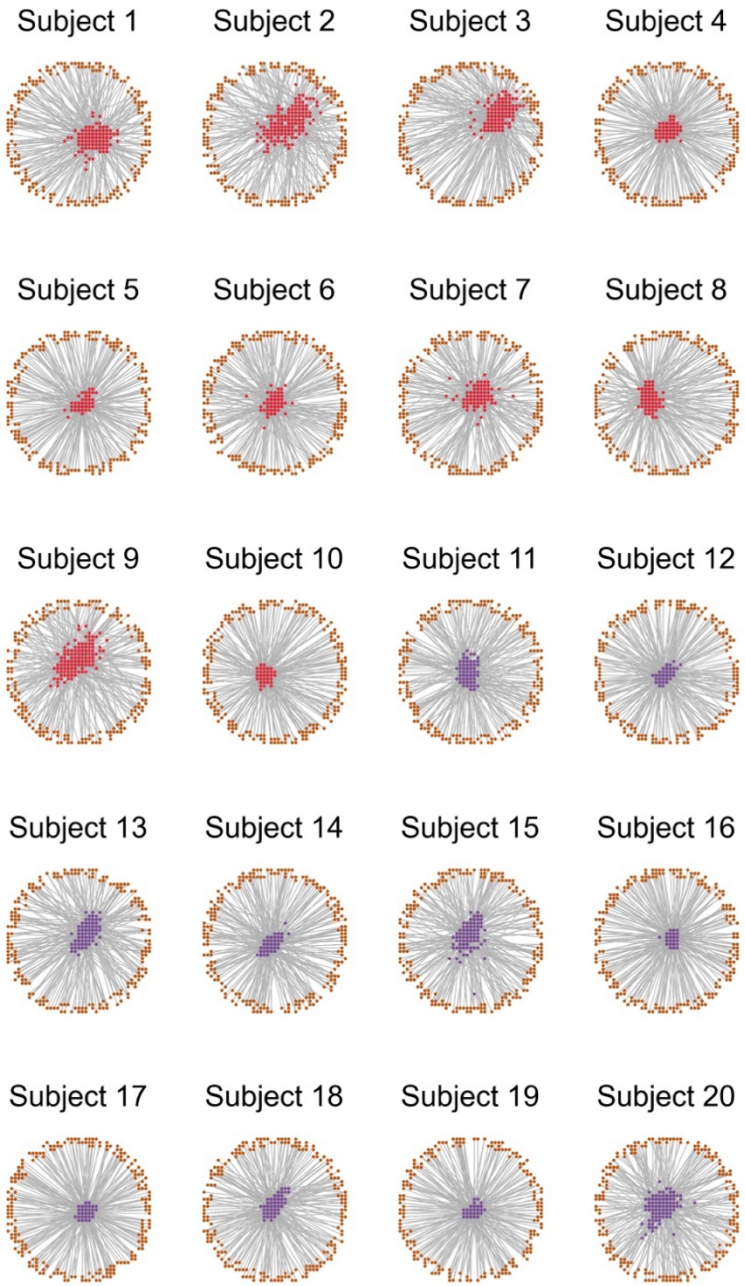

Figure S3. Distribution of hexagonal orientations in the ERC of the experimental (red) and replication (purple) group. The uniformity of hexagonal orientations, which was computed from each voxel, was tested by Rayleigh test. All participants showed significantly clustered hexagonal orientations ($p < 0.05$, Bonferroni corrected). The length of bars indicates the number of voxels and the black line denotes the mean of hexagonal orientations.

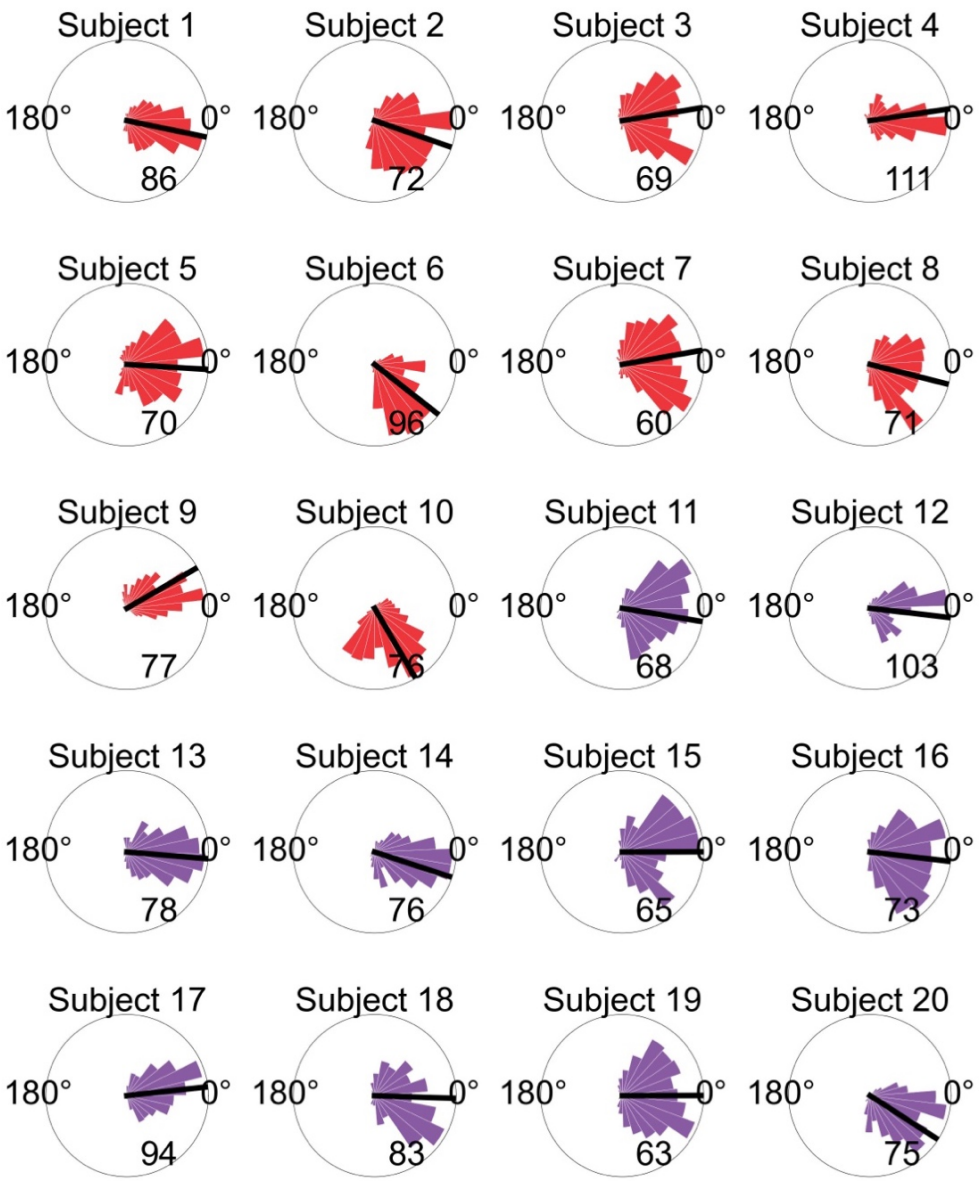

Figure S4. Neural periodicity of the ERC and the HPC observed in the replication group. The 6- and 3-fold modulation, revealed by sinusoid and spectral analysis, was revealed in the right ERC and the right HPC, respectively (initial threshold: $p < 0.01$; SVC for multiple comparisons: $p < 0.05$). Error bar denotes SEM.

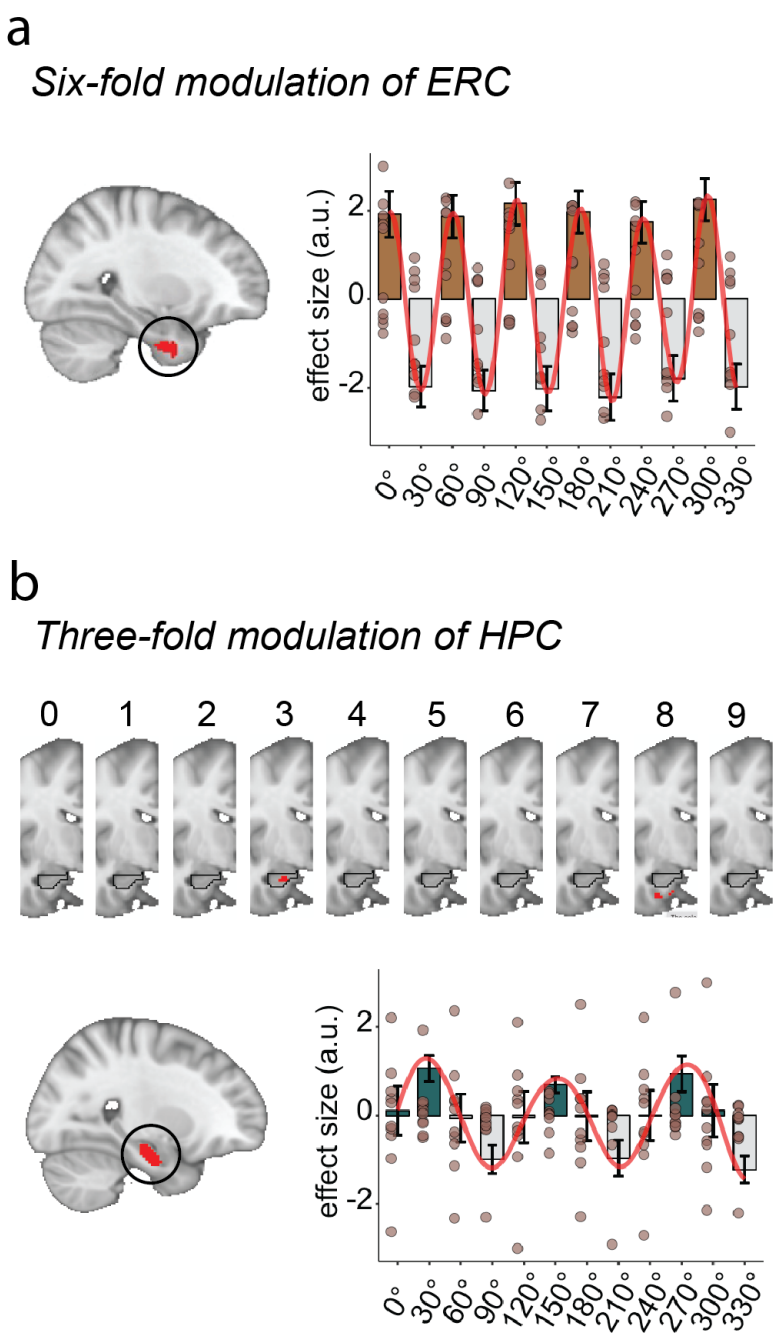

Figure S5. The 3-fold modulation of the HPC examined using 10° and 20° bin. The significant clusters were robustly revealed in the right HPC (initial threshold on pseudo t-value: $p < 0.05$; SVC for multiple comparison: $p < 0.05$). The x & y value denote MNI coordinate.

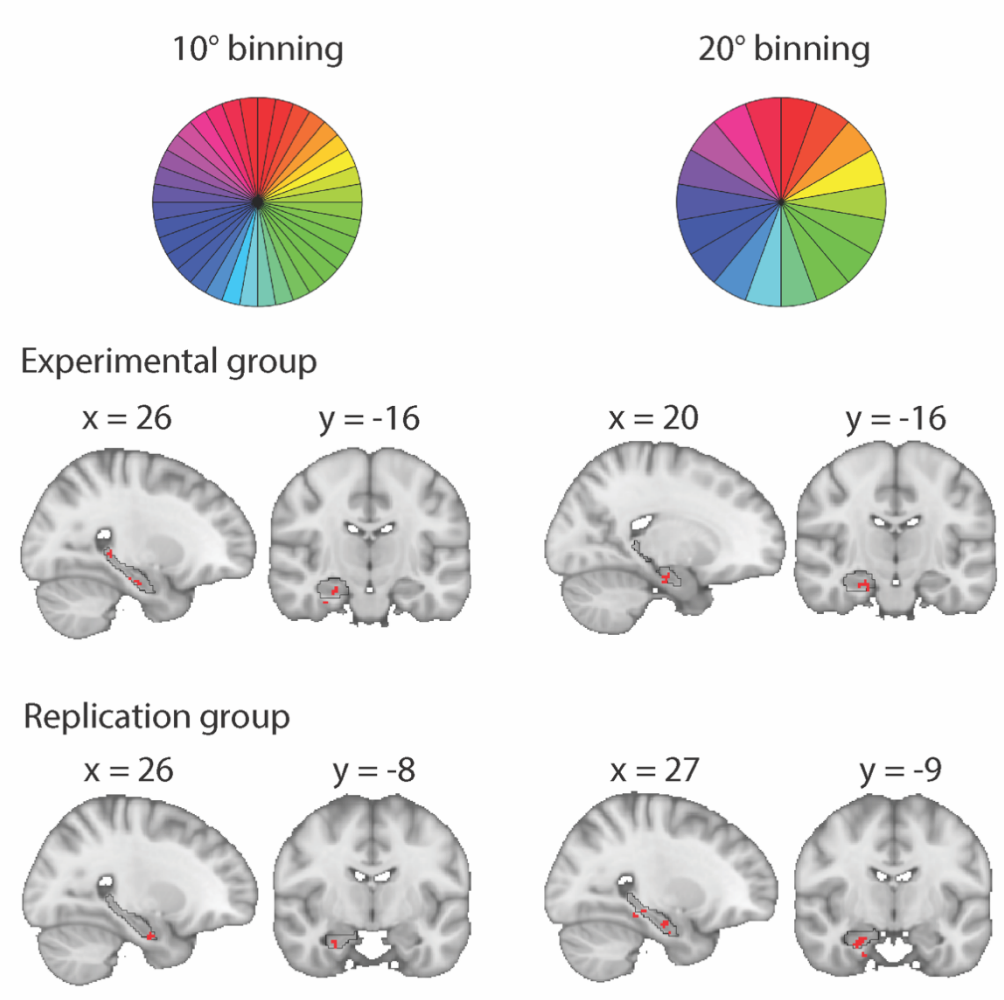

Figure S6. BOLD signals of the ERC (black) and HPC (red & purple denoting the experimental and replication group, respectively) fluctuate as a function of conceptual directions (0°-360°; shown on x-axis).

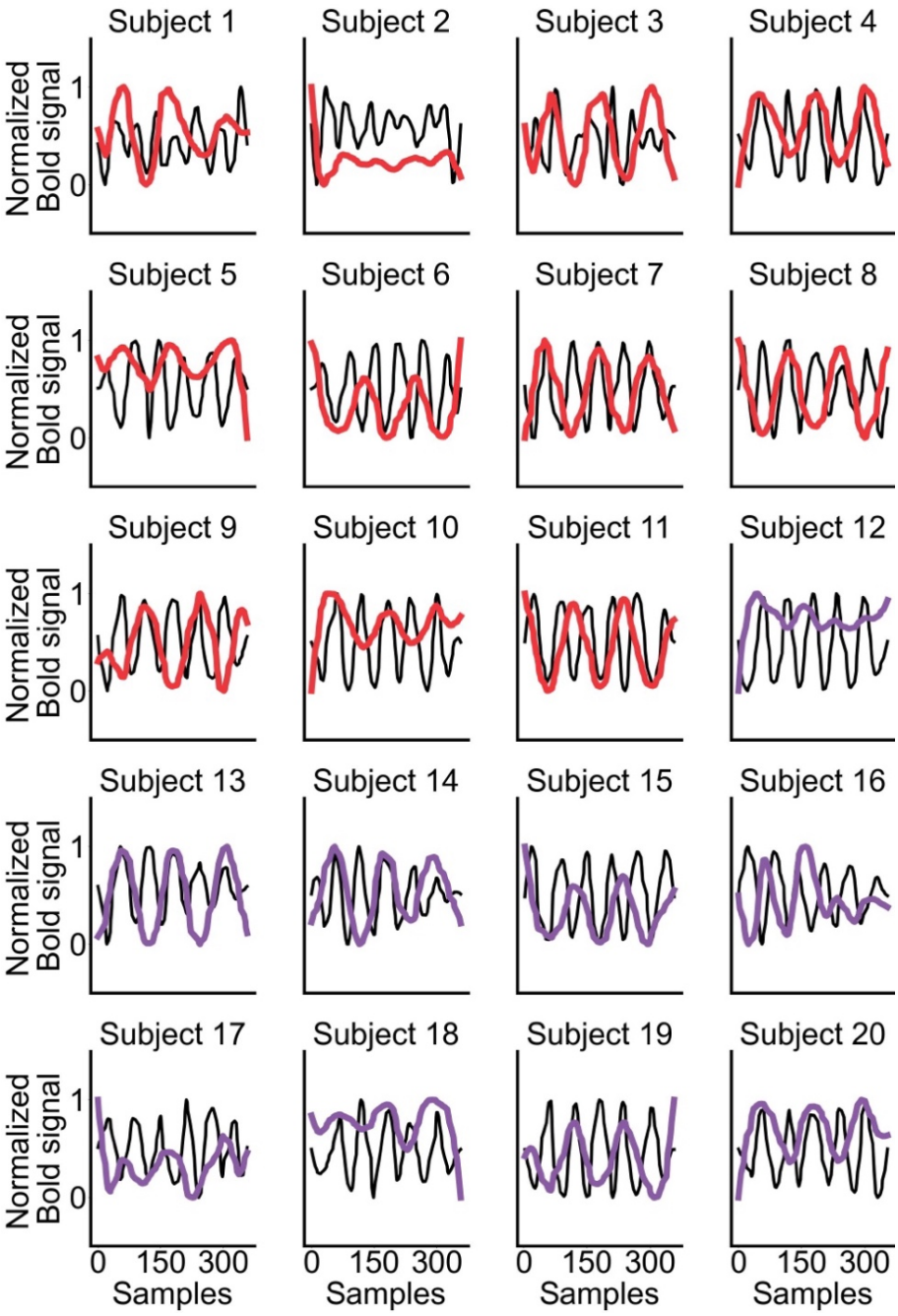
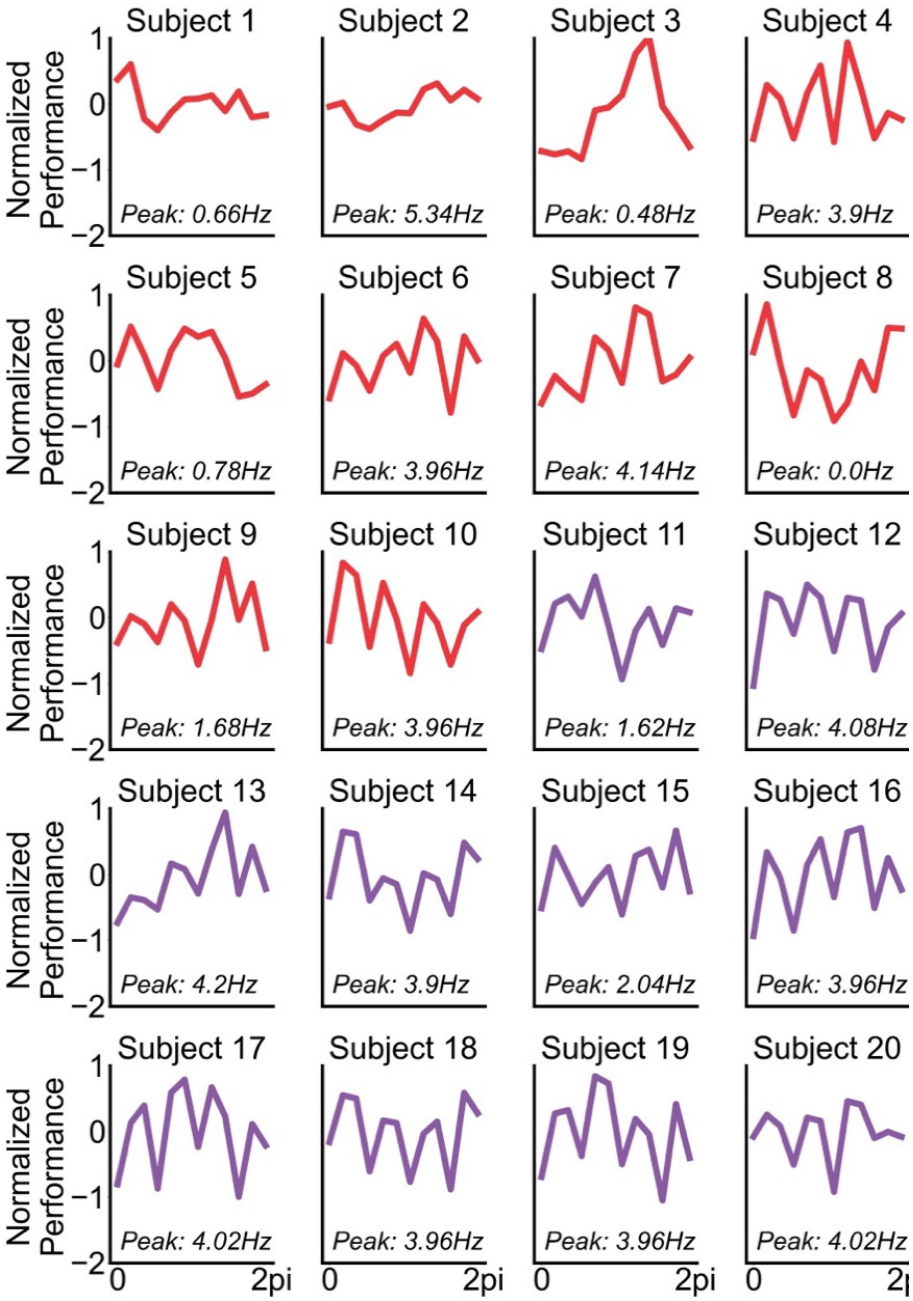
Figure S7. Raw behavioral performances of human participants from the experimental (red) and replication (purple) group change as a function of conceptual directions (0 to 2pi shown on x-axis).